Contrib Mineral Petrol (2015) 169:49
DOI 10.1007/s00410-015-1145-4

ORIGINAL PAPER

To the origin of Icelandic rhyolites: insights from partially melted leucocratic xenoliths

Andrey A. Gurenko[1,2,3] · Ilya N. Bindeman[4] · Ingvar A. Sigurdsson[5]

Received: 23 December 2014 / Accepted: 30 April 2015 / Published online: 20 May 2015

Abstract We have studied glass-bearing leucocratic (granitic to Qz-monzonitic) crustal xenoliths from the Tindfjöll Pleistocene volcanic complex, SW Iceland. The xenoliths consist of strongly resorbed relicts of anorthitic plagioclase, K-rich feldspar and rounded quartz in colorless through pale to dark-brown interstitial glass. Spongy clinopyroxene and/or rounded or elongated crystals of orthopyroxene are in subordinate amount. Magnetite, ilmenite, zircon, apatite, allanite and/or chevkinite are accessory minerals. The xenoliths more likely are relicts of earlier-formed, partially melted Si-rich rocks or quartz–feldspar-rich crystal segregations, which suffered latter interaction with hotter and more primitive magma(s). Icelandic lavas are typically low in δ^{18}O compared to mantle-derived, "MORB"-like rocks (~5.6 ± 0.2 ‰), likely due to their interaction with, or contamination by, the upper-crustal rocks affected by rain and glacial melt waters. Surprisingly, many quartz and feldspar crystals and associated colorless to light-colored interstitial glasses of the studied xenoliths are not low but high in δ^{18}O (5.1–7.2 ‰, excluding three dark-brown glasses of 4–5 ‰). The xenoliths contain abundant, low- to high-δ^{18}O (2.4–6.3 ‰) young zircons (U–Pb age 0.2–0.27 ± 0.03 Ma; U–Th age 0.16 ± 0.07 Ma), most of them in oxygen isotope equilibrium with interstitial glasses. The δ^{18}O values >5.6 ‰ recorded in the coexisting zircon, quartz, feldspar and colorless interstitial glass suggest crystallization from melts produced by fusion of crustal rocks altered by seawater, also reflecting multiple melting and crystallization events. This suggests that "normal"-δ^{18}O silicic magmas may not be ultimately produced by crystallization of mafic, basaltic magmas. Instead, our new single-crystal laser fluorination and ion microprobe O-isotope data suggest addition of diverse partial crustal melts, probably originated from variously altered and preconditioned crust.

Keywords Iceland · Rhyolites · Leucocratic xenoliths · Oxygen isotopes · Zircon age

Communicated by Timothy L. Grove.

Electronic supplementary material The online version of this article (doi:10.1007/s00410-015-1145-4) contains supplementary material, which is available to authorized users.

✉ Andrey A. Gurenko
agurenko@crpg.cnrs-nancy.fr

[1] Present Address: Centre de Recherches Pétrographiques et Géochimiques, UMR 7358, Université de Lorraine, 15 rue Notre-Dame des Pauvres, BP 20, 54501 Vandoeuvre-lès-Nancy, France

[2] Geology and Geophysics, Woods Hole Oceanographic Institution, Woods Hole, MA 02543, USA

[3] Max-Planck-Institut für Chemie, Hahn-Meitner-Weg 1, 55128 Mainz, Germany

[4] Department of Geological Sciences, 1272 University of Oregon, Eugene, OR 97403, USA

[5] South Iceland Nature Centre, Strandvegur 50, Vestmannaeyjar 900, Iceland

Introduction

Silicic magmas play a fundamental role in the origin of the continental crust. Whether Icelandic silicic magmas predominantly result from promoted fractionation of parental basaltic magmas (e.g., Bowen 1928; Carmichael 1964; Gerasimovsky et al. 1978; Macdonald et al. 1987, 1990; Furman et al. 1992; Prestvik et al. 2001; Namur et al. 2011; Portnyagin et al. 2012) or they originate during partial melting of older, metamorphosed oceanic

crust (e.g., Sigurdsson 1977; Thy et al. 1990; Sigmarsson et al. 1991, 1992; Gunnarsson et al. 1998; Bindeman et al. 2008a, 2012, 2014; Gillis and Coogan 2002; Jónasson 2007; Sverrisdottir 2007) is still a subject of debate. Silicic rocks constitute 5–10 % of all igneous rocks in Iceland (Walker 1966; Jónasson 2007). It is by approximately a factor of 2 higher than could be produced by fractional crystallization alone (McBirney 2006). There are several petrogenetic hypotheses for the origin of silicic magmas in Iceland (see Gunnarsson et al. 1998): (1) pure fractional crystallization of basaltic magma, (2) fractional crystallization coupled with remelting of the crust followed by magma mixing, (3) partial melting of hydrothermally altered basalt or amphibolite of layer 3, (4) remelting of earlier-formed MORB-like plagiogranites, crystal segregations from the periphery of solidifying basaltic intrusions and/or subsided evolved intrusives and lavas beneath the core of large long-lived central volcanoes. Martin and Sigmarsson (2007) have demonstrated recently that silicic magmas within, or close to, the Icelandic neovolcanic rift zone are preferentially formed by crustal melting, whereas the origin of lavas erupted off the rift zones can be better explained by fractional crystallization. In addition, many Icelandic lavas exhibit systematically lower δ^{18}O values than those traditionally ascribed to mantle-derived rocks (i.e., lower than 5.2–5.6 ‰), due to their interaction with, or contamination by, upper-crustal rocks affected by rain and glacial melt waters (e.g., Muehlenbachs et al. 1974; Hattori and Muehlenbachs 1982; Condomines et al. 1983; Gautason and Muehlenbachs 1998). As previously shown by Gurenko and Chaussidon (2002) and Bindeman et al. (2008a, 2012), both large-volume basaltic and evolved silicic lavas in Iceland contain strongly δ^{18}O-diverse olivines and zircons. This suggests that assimilation of hydrothermally altered, isotopically diverse crustal rocks and crustal anatexis is likely very common in Iceland.

The abundant partially melted leucocratic xenoliths quenched at different stages of fusion have been described previously in the products of many recent eruptions in Iceland (e.g., Jakobsson 1966; Sigurdsson 1968, 1977; Sigurdsson and Sparks 1981; Blake 1984; Macdonald et al. 1987; Jørgensen 1987; Lacasse et al. 2007). The majority of these xenoliths show compositional affinity with oceanic plagiogranites and range from trondhjemites (i.e., tholeiitic rocks usually containing no K-feldspar) to granodiorites (more alkali-rich composition, K-feldspar is present), whereas chemical composition of interstitial glasses from these xenoliths is broadly similar to the Icelandic rhyolites, suggesting their close genetic link (Sigurdsson 1968, 1977; Sigurdsson and Sparks 1981; Macdonald et al. 1987).

We studied glass-bearing leucocratic xenoliths collected to the south of the Hungurfit tuff cone, in the Tindfjöll Pleistocene volcanic complex (Fig. 1a). These xenoliths were supplied by basaltic andesite to andesite hyaloclastites and range chemically from granite to quartz-monzonite. Special attention was given to particularly this type of xenoliths because they contain enormous amount of zircons (tens to hundreds individual zircon grains of ~20 to ~100 μm size can be extracted from only a few gram of the host rock). As zircon is very resistant to secondary alteration and mechanical abrasion, it is often present in the younger lavas as a xenogenic phase accumulated in a magma chamber during precursor crustal anatexis events, along with zircons immediately crystallized from the melt (Bindeman and Simakin 2014; Bindeman et al. 2008b, 2012). We present the results of a detailed geochemical study (major, trace element and oxygen isotope compositions of the coexisting nodule-forming minerals and interstitial glasses) and of zircon dating, with an ultimate aim to unravel the processes that govern the origin of silicic magmas in Iceland. Special attention is given to possible contribution of hydrothermally altered crustal rocks to magma formation.

Geological setting

The upper Pleistocene Tindfjöll volcanic system (<0.7 Ma, total area ~360 km^2) is situated in the western part of the currently active Eastern Volcanic Zone (EVZ) of Iceland, south of Hekla and Vatnafjöll (Fig. 1a). The Tindfjöll volcanic system is superimposed on the older Tertiary crust ~4 My ago and mainly formed during the last three glaciations and last two interglacial periods (e.g., Palmason and Saemundsson 1974; Jakobsson 1979). Tindfjöll is composed of basaltic, rhyolitic and less frequent andesitic lavas, hyaloclastites and dykes having transitional to alkali affinity (Jakobsson 1972; Larsen 1979). Aphyric transitional basaltic rocks dominate the lower parts of the complex, intermediate and acid rocks are intercalated. A caldera, ~5 km in diameter, was formed during the early history of the volcanic complex. The Thórsmörk ignimbrites originate within the Tindfjöll caldera, date the second last interglacial period in Iceland and are composed of two, a dominating salic (comenditic) and a subordinating basic (mugearitic), magma components (Jørgensen 1980). During the last interglacial and glacial periods, a variety of basaltic to peralkaline rhyolitic lavas erupted as within the caldera, as on the flanks of the volcano. The youngest rocks of the Tindfjöll system are characterized predominantly by basaltic composition (Jakobsson 1979). No eruptions from historical time are known in the Tindfjöll system.

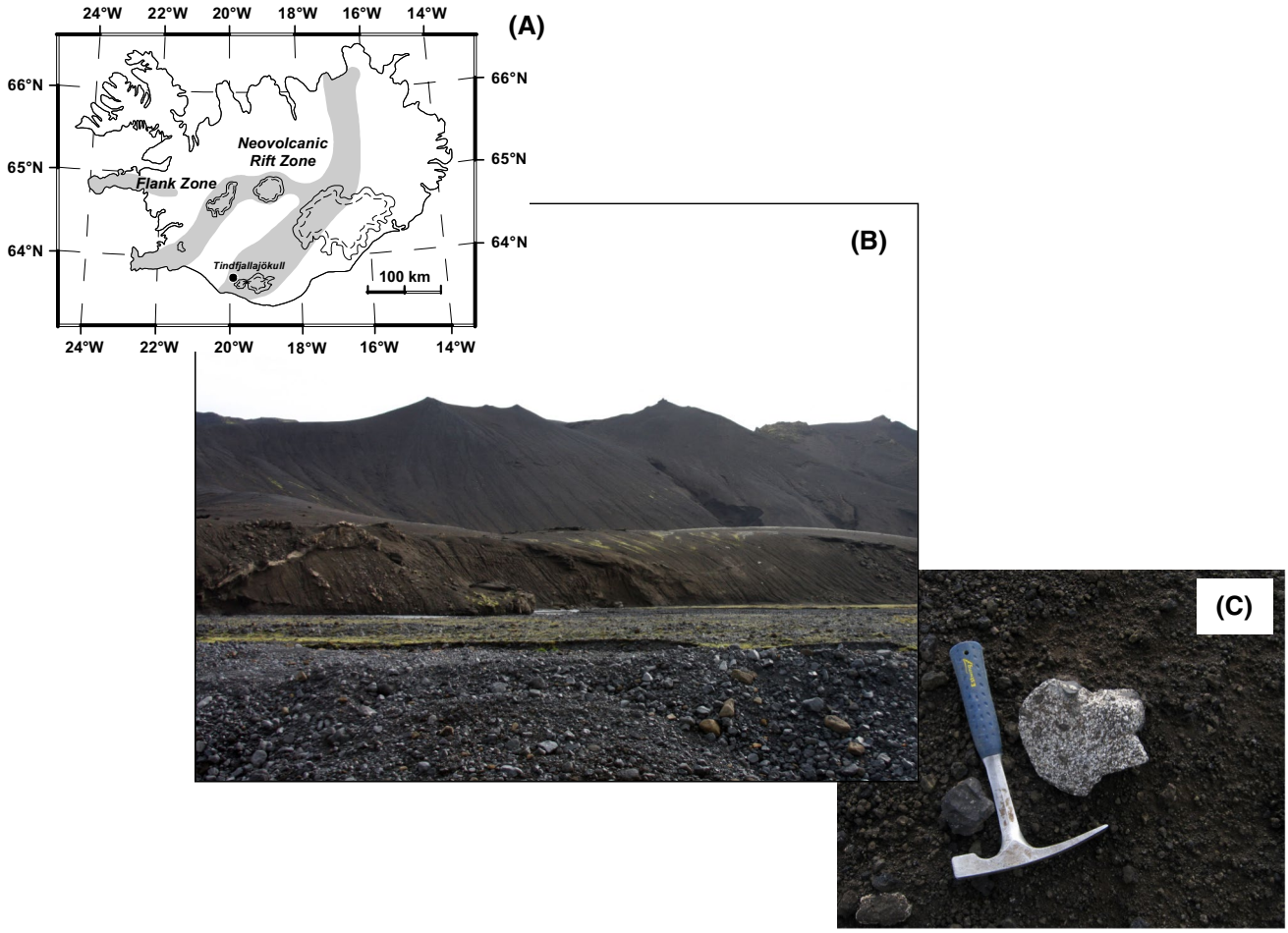

Fig. 1 **a** Schematic map of Iceland showing the location of the Tindfjöll Pleistocene volcanic complex in the southern part of the currently active Eastern Volcanic Zone. **b** A view of the hyaloclastite ridge located to the south of the Hungurfit tuff cone (63°49.83′N 19°32.58′W). **c** Loose leucocratic xenolith on the surface of the transporting hyaloclastite

Sample description

Petrography and mineral composition

Abundant loose crustal nodules (gabbroic and leucocratic) with interstitial glass and outer chilled glassy crusts occur along the top of a hyaloclastite ridge of subglacial origin located near the Hungurfit volcanic cone (63°49.83′N 19°32.58′W) (Fig. 1b, c). We focus exclusively on the leucocratic xenoliths. The size of the studied xenoliths ranges from a few up to 20 cm, with the majority at ~10 ± 5 cm. Most of them have granular texture. The xenoliths are composed of rounded, often strongly resorbed and spongy anorthitic plagioclase (Pl) and K-rich feldspar (Fsp, $Ab_{21–80}$ $An_{1–37}$ $Or_{1–78}$; up to 60 vol% and size of 2–3 mm), rounded, moderately to strongly resorbed quartz (Qz, up to 20 vol% and size of 1–2 mm) and variable amounts (30–80 vol%) of either homogeneous pale to brown (IC03-130-15) or mingling colorless through pale or light brownish to dark-brown glass matrix (all other samples) (Fig. 2; Tables B1–B6; *Supporting Online Material*). Spongy aggregates and resorbed individual grains of clinopyroxene (Cpx, mg# = 52–68, $Wo_{34–43}$ $En_{31–46}$ $Fs_{16–27}$) and/or elongated, often needle-like, skeletal crystals of orthopyroxene (Opx; mg# = 62–75, $Wo_{1–10}$ $En_{58–77}$ $Fs_{20–36}$) in amount of <5 vol% (Fig. 2a, e, f) are observed in all studied xenoliths. They are spatially associated with patches of Fe–Ti oxides surrounded by the darker, pale to brownish glass but never present in the colorless glass. Magnetite ($Spl_{1–9}$ $Mag_{58–84}$ $Usp_{14–37}$) is present as dispersed in glass, individual crystals and as segregations of several tens of grains. Some individual Fe–Ti oxide grains can be surrounded by a halo of brownish glass that suggests their dissolution (Fig. 2b, c). Multiple zircon (Zrn) and rare ilmenite crystals ($Ilm_{53.6–77.8}$ $Hem_{22.2–46.4}$) are found adherent to these segregations, together with rare

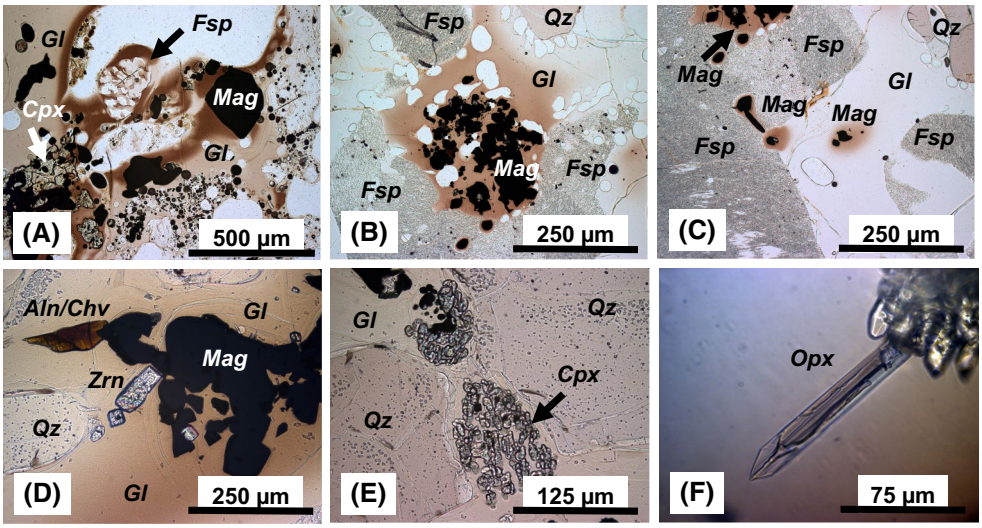

Fig. 2 Typical textures of the studied leucocratic xenoliths (on example of sample IC03-130-14). **a** Strongly resorbed, partially melted feldspar (Fsp), relicts of spongy clinopyroxene (Cpx) and rounded magnetite (Mag) crystals in a matrix of vesiculated, mingling dark, brownish and light-colored, yellowish interstitial glass (Gl) matrix. **b** A cluster of multiple Fe–Ti oxide grains (mostly Mag) in a pool of brownish glass surrounded by partially melted, spongy Fsp and rounded Qz grains in vesiculated colorless interstitial glass. **c** Individual Fe–Ti oxide grains with a halo of brownish glass, sponge Fsp and rounded Qz grains in colorless interstitial glass. **d** A cluster of Fe–Ti oxide grains and associated zircon (Zrn), allanite (Aln) or chevkinite (Chv) crystals in brownish interstitial glass. **e** Two resorbed spongy Cpx relicts between two larger Qz grains in pale interstitial glass. **f** Idiomorphic, strongly elongated orthopyroxene (Opx) in brownish interstitial glass

grains or elongated crystals of optically unzoned, intense brown Ti-rich silicate mineral with high relief and high birefringence, resembling allanite (Aln) or chevkinite (Chv)—both minerals were described in the alkaline granophyric xenoliths from Thórsmörk by Jørgensen (1987) (Fig. 2d). Rare elongated apatite (Ap) crystals are also present. No amphibole was detected.

The transporting hyaloclastites (Table B2; *Supporting Online Material*) are presented by fresh and altered pale to yellowish moderately consolidated vesicular glass shards and pumice fragments, sometimes with adhering crusts of dark brownish glass, and by loose glassy lapillis mixed up with glomerocrysts and individual crystals and crystal fragments of plagioclase, K-feldspar, pyroxene and rare olivine.

Zircon morphology and zoning

Zircons are very abundant but relatively small (a few tens to ~100 µm). Predominately euhedral, elongated crystal shapes (well faceted to slightly resorbed crystals with length-to-height ratio, L/H ≈ 2–3) and subtle, low-contrast back-scattered electron (BSE) and cathodoluminescent (CL) element distribution patterns (lack of well-defined cores, oscillatory zoning barely visible) are typical and similar from grain to grain and from sample to sample, suggesting their simple magmatic history.

Results

Major and trace element geochemistry

Major and trace element concentrations of the studied xenoliths (whole-rock compositions) and their interstitial glasses are presented in Figs. 3, 4 and 5 (for analytical technique details, see Appendix A and for chemical compositions—Appendix B, *Supporting Online Material*). Xenoliths form two distinct clusters, matching the compositional fields of granites and Qz-monzonites in the "total alkalis-silica" (TAS) diagram (Fig. 3), in accordance with IUGS classification of igneous rocks (Le Bas et al. 1986; Le Bas and Streckeisen 1991). Interstitial glasses, which include colorless, pale and brown types, are characterized by similar chemical composition ranging from rhyolite to trachydacite (Fig. 3). The agpaitic index ($[Na_2O + K_2O]/Al_2O_3$, molar ratio) of the host xenoliths and their interstitial glasses lies in the same interval, from significantly below to about unity (0.71–0.95 and 0.8–1.03, respectively), suggesting their overall metaluminous affinity, contrary to the neighboring, slightly peralkaline rhyolites from Torfajökull, with agpaitic index of 1.00–1.15 (Gunnarsson et al. 1998; Martin and Sigmarsson 2007). The transporting hyaloclastites (two samples) are more mafic, resembling basaltic andesite and andesite, in accordance with IUGS classification of igneous rocks (Le Bas et al. 1986; Le Bas

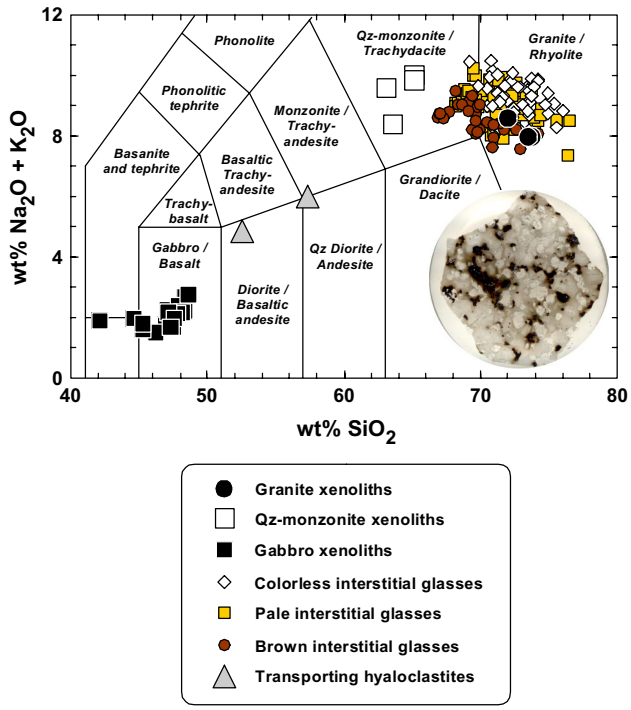

Fig. 3 Total alkali versus SiO_2 of the studied leucocratic xenoliths, interstitial glasses and transporting hyaloclastites. The IUGS reference fields of effusive rocks and their intrusive analogs are from Best (2003). The compositions of spatially associated gabbroic xenoliths (authors' unpublished data) are given for comparison. The *inset* (original size 25 mm) presents texture of sample IC03-130-14, which is typical for most studied xenoliths

and Streckeisen 1991); they also are called transitional mugearite and benmoreite according to Jakobsson et al. (2008) (Fig. 3).

We observe a general tendency of systematic decrease in TiO_2, FeO and Zr concentrations with increasing SiO_2 in the sequence of interstitial glass types, from brown through pale to colorless glasses (Fig. 4a–c). There is also a clear difference between the granite and Qz-monzonite types of xenoliths with respect to these element concentrations. Other major elements show no systematic change and demonstrate similar concentration ranges regardless of the xenolith's type. Similarly, no systematic difference in major element concentrations was observed between different types of interstitial glasses. However, brown, pale and colorless interstitial glasses from two of three granite xenoliths (i.e., IC03-130-18 and IC03-130-19) are characterized by systematically lower Zr and Ba and varying to significantly higher Th, with Zr/Th ≈ 12.5 and Ba/Th ≈ 5. In contrast, the other xenoliths show relatively low Th and varying to high Zr and Ba, with Zr/Th ≈ 125 and Ba/Th ≈ 80 (Fig. 4d, e).

As shown in primary-mantle normalized multi-element diagrams (Fig. 5), interstitial glasses, their host xenoliths and transporting hyaloclastites have several common features in trace element concentrations and ratios:

1. Overall enrichment in strongly incompatible trace elements ($[La/Sm]_n$ = 0.7–5.6 in interstitial glasses, $[La/Sm]_n$ = 2.1–6.5 in host xenoliths and $[La/Sm]_n$ = 2.4–2.5 in transporting hyaloclastites) accompanied by strongly varying to high Zr concentrations up to 2000 μg/g. As discussed below, saturation and immediate crystallization of zircons from interstitial, preferentially dark-colored melts can be ascribed to such elevated Zr concentrations.
2. The presence of significant depletion in Pb, Sr, Eu and Ti concentrations relative to other trace elements of similar incompatibility ($[Pb/Ce]_n$ = 0.18–0.69, $[Sr/Nd]_n$ = 0.004–0.035, $[Eu/Sm]_n$ = 0.1–0.71 and $[Ti/Gd]_n$ = 0.02–0.09 in interstitial glasses, $[Pb/Ce]_n$ = 0.26–0.72, $[Sr/Nd]_n$ = 0.04–0.16, $[Eu/Sm]_n$ = 0.34–0.97 and $[Ti/Gd]_n$ = 0.05–0.18 in host xenoliths, and $[Pb/Ce]_n$ = 0.33–0.39, $[Sr/Nd]_n$ = 0.38–0.53, $[Eu/Sm]_n$ = 0.77–0.78 and $[Ti/Gd]_n$ = 0.49–0.8 in transporting hyaloclastites), except for the colorless and brown interstitial glasses from sample IC03-130-19 ($[Pb/Ce]_n$ = 1.4 and 1.34, respectively). This may point toward extensive fractionation of feldspar and Fe–Ti–rich oxides from the magma or, in contrast, latter feldspar and Fe–Ti–rich oxide control during consequent melting of silicic crustal bodies, or reflect a cumulative impact of both processes.
3. One of the seven samples, IC03-130-02, and its interstitial glasses are characterized by significantly lower trace element concentration and show remarkably different element ratios and the highest Zr enrichment in the multi-element diagrams (i.e., $[Pb/Ce]_n$ = 0.59–0.66, $[Sr/Nd]_n$ = 0.18–0.2, $[Eu/Sm]_n$ = 1.3–1.4, $[Zr/Sm]_n$ = 4.95–7.44 and $[Ti/Gd]_n$ = 0.25–0.41 in interstitial glasses and $[Pb/Ce]_n$ = 0.96, $[Sr/Nd]_n$ = 1.3, $[Eu/Sm]_n$ = 4.3, $[Zr/Sm]_n$ = 18.3 and $[Ti/Gd]_n$ = 0.7 in the host xenolith).
4. The granite xenoliths along with their transporting hyaloclastites demonstrate slight depletion to significant enrichment in Nb relatively to Ba and La ($[Nb/Ba]_n$ = 0.98–20.9 and $[Nb/La]_n$ = 0.71–7.4 in interstitial glasses, $[Nb/Ba]_n$ = 1.99–2.63 and $[Nb/La]_n$ = 1.02–1.32 in host xenoliths and $[Nb/Ba]_n$ = 1.53–1.72 and $[Nb/La]_n$ = 1.14 in the transporting hyaloclastites), whereas the Qz-monzonite xenoliths display overall depletion in Nb relatively Ba and La ($[Nb/Ba]_n$ = 0.22–2.83 and $[Nb/La]_n$ = 0.36–2.38 in interstitial glasses, and $[Nb/Ba]_n$ = 0.11–0.86 and $[Nb/La]_n$ = 0.34–1.58 in host xenoliths). This may suggest an allanite/chevkinite control during magma crystallization or, in contrast, their partial melting since

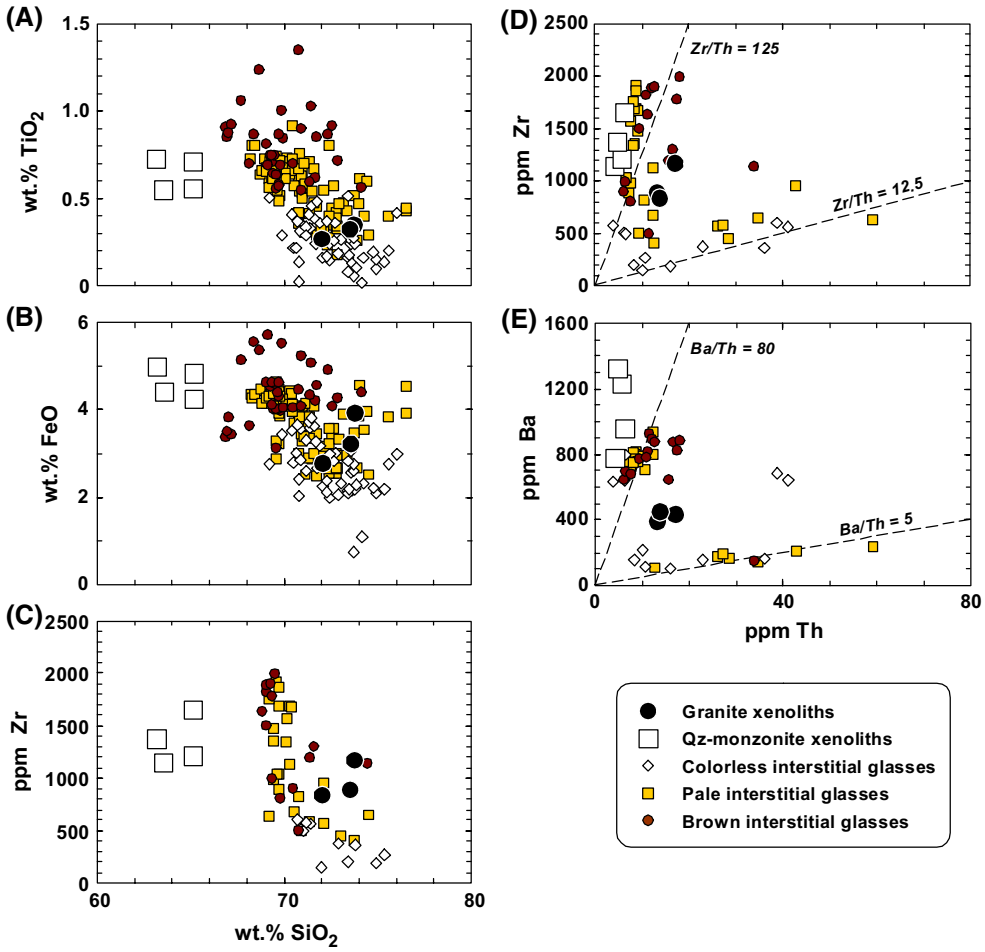

Fig. 4 Chemical composition of colorless, pale and brown interstitial glasses given in comparison with their host xenoliths, presented in **a** TiO_2, **b** FeO and **c** Zr versus SiO_2, and **d** Zr and **e** Ba versus Th variation diagrams. There is no systematic difference in major element concentrations, as between different types of interstitial glasses, as between the glasses from the granite and Qz-monzonite xenolith types. Two different groups of interstitial glasses can be selected based on their Zr/Th and Ba/Th ratios (see text)

these accessories is a major inventory of Y, Zr, Nb and rare earth elements in the evolved, silica-rich magmas.

Temperature and redox conditions

The temperature (T) and oxygen fugacity (f_{O_2}) conditions of the xenolith formation and possible interaction with the transporting magma were estimated by (1) mineral geothermometry based on the equilibrium between coexisting Opx, Cpx and Fe–Ti oxides, using a QUILF program (Andersen et al. 1993) with calibrations of Andersen and Lindsley (1988) and Frost et al. (1988), (2) two-pyroxene geothermometer (Lindsley 1983), (3) experimental data on the temperature of melt saturation with zircon (Watson and Harrison 1983; Boehnke et al. 2013) and (4) Ti-in-zircon thermometry (Watson and Harrison 2005; Watson et al. 2006; Ferry and Watson 2007).

Because Opx, Cpx, Mag and Ilm do not always coexist as a four-mineral association in each of the studied xenoliths, we used QUILF in two different calculation modes: (a) a two-pyroxene mode (assigning Mag and Ilm compositions to estimate f_{O_2}) for the samples where both Opx and Cpx are present (IC03-130-14 and -16), and (b) in a single-pyroxene mode, using either Cpx or Opx compositions, also including compositions of Mag and Ilm in the calculations. A similar approach to use QUILF in the single-pyroxene mode was employed by Murphy et al. (1998) and Gurenko et al. (2005).

To use QUILF in the single-pyroxene mode, the activity of SiO_2 in the melt must be assigned. QUILF can routinely calculate it along with T and f_{O_2}, only if compositions of coexisting Opx and Cpx are known. Thus, our calculations included two steps. First, the activity of SiO_2 was calculated substituting average compositions of Opx

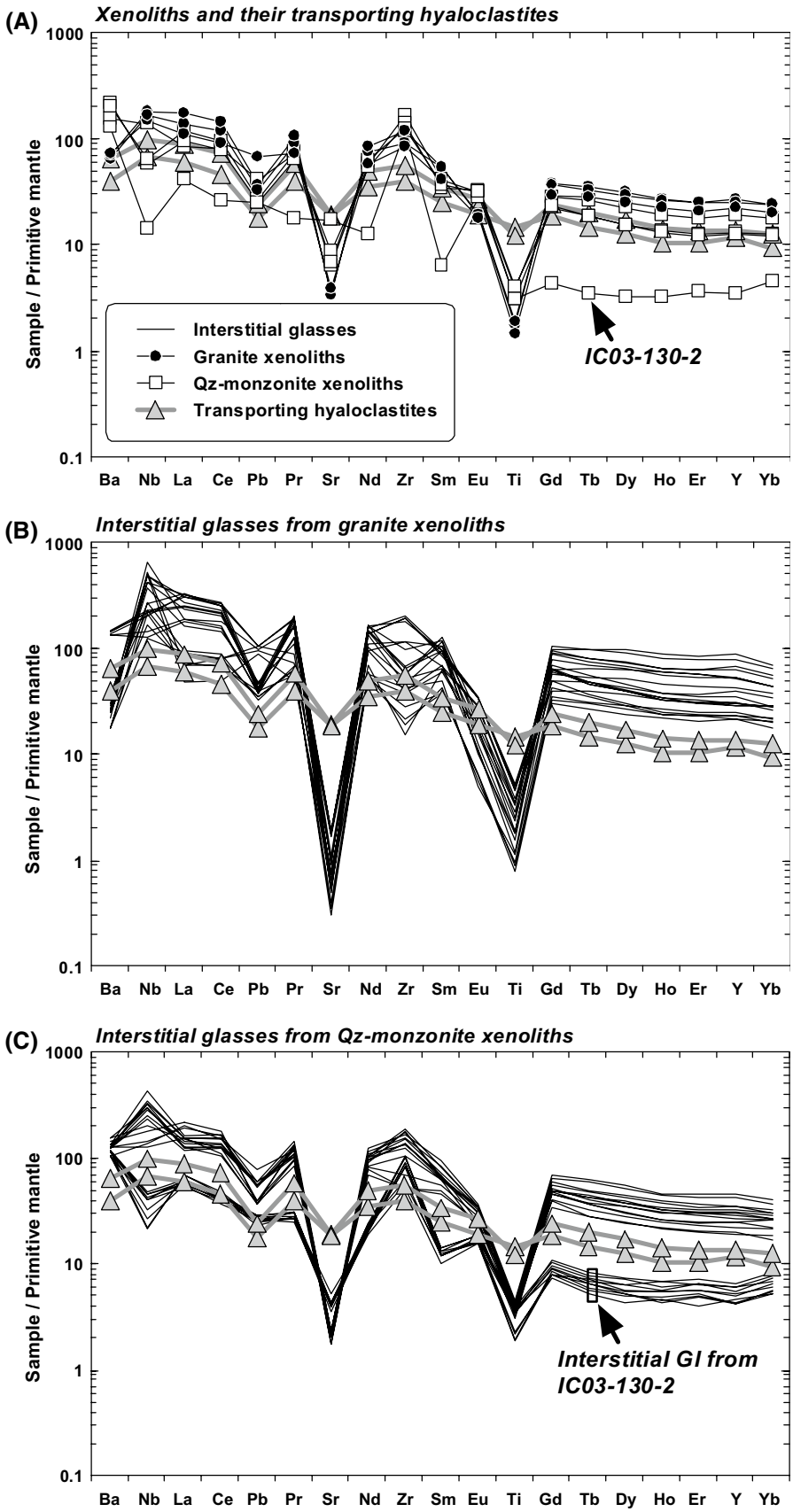

Fig. 5 Multi-element diagrams outlining trace element composition of the studied leucocratic xenoliths and their transporting hyaloclastites (**a**), interstitial glasses from granitic (**b**) and from Qz-monzonitic (**c**) xenolith types. Concentrations of trace elements in primitive mantle used for normalization are from Hofmann (1988)

or Cpx, whatever phase is absent in the sample. Then, to calculate temperature, we switched QUILF in the single-pyroxene mode, substituting a_{SiO_2} estimated during the first step. The calculated a_{SiO_2} values range from 0.98 to 1 in granite xenoliths and from 0.83 to 1 in more alkali-rich Qz-monzonite xenoliths (Table 1), in accordance with the presence of quartz in all studied xenoliths. Although the uncertainty of T calculation using the QUILF single-pyroxene mode is somewhat higher, as compared to when the compositions of coexisting Opx and Cpx are available, this approach provides broadly consistent T-ranges, as shown for samples IC03-130-14 and IC03-130-16 (Table 1). Since ilmenite was analyzed only in two of 7 xenoliths, in Qz-monzonite IC03-130-17 and in granite IC03-130-19, we also used two average ilmenite compositions (one for the other three Qz-monzonite and the second for the other two granite xenoliths) to calculate T and f_{O_2} conditions. Our QUILF calculations yield the following intervals of temperature (average uncertainty ±45 °C) and oxygen fugacity (average uncertainty ±0.5 log atm. units f_{O_2}) calculated for 1 atm. total pressure (Fig. 6):

1. Two of 3 granite xenoliths (IC03-130-14, IC03-130-18) are characterized by similar, overlapping but systematically higher T-ranges from ~1070 to ~1150 °C and from 1020 to 1205 °C, respectively, as compared to the third xenolith (IC03-130-19) showing T-range from ~890 to 1010 °C.
2. Similarly, the redox conditions also systematically differ between these samples. Xenoliths IC03-130-14 and IC03-130-18 are characterized by f_{O_2} conditions ranging from −8.0 to −7.1 and from −8.4 to −5.9 log atm., respectively [ΔFMQ defined as $\log(f_{O_2})_{sample} - \log(f_{O_2})_{FMQ}$ at a given temperature] ranges from 1.8 to 2.3 and from 1.9 to 2.6 log atm., respectively. In contrast, sample IC03-130-19 is characterized by more oxidized conditions, i.e., f_{O_2} ranging from −9.9 to −8.2 log atm. (ΔFMQ from 2.7 to 3.1 log atm.).
3. Qz-monzonite xenoliths (samples IC03-130-2, IC03-130-15, IC03-130-16 and IC03-130-17) are characterized by similar, overlapping T-ranges from ~880 to ~1020 °C and f_{O_2} conditions ranging from −11 to −9.6 log atm. (ΔFMQ from 1.2 to 2.1 log atm., except to one estimation of 2.8 log atm.).

The graphical version of the two-pyroxene geothermometer (Lindsley 1983) returns similar wide ranges, but systematically lower absolute temperatures (from ~900 to ~1100 °C for granite xenoliths and from ~700 to 1000 °C for Qz-monzonite xenoliths; Fig. 7). Taking into account high uncertainty of the geothermometer graphical version (about ±100 °C, if the uncertainty of chemical composition and crystallographic formula calculations are considered), we think that temperatures calculated by QUILF represent more precise estimations.

Temperature of zircon saturation and growth

The zircon saturation temperatures ($T_{Zrn\text{-}sat}$) were calculated using the revised equation of the zircon solubility model (Boehnke et al. 2013) that gives the uncertainty of ±30–50 °C, if combining (a) the uncertainties assigned for the constants in the working equation and (b) ±10 % analytical precision of Zr analysis by LA ICP-MS. The new data of Boehnke et al. (2013) have yielded broadly similar solubility patterns as that of Watson and Harrison (1983) and confirmed that the "melt basicity" factor ($M = [Na + K + 2Ca]/[Al \times Si]$, atomic fraction) is an important parameter to account for dependence of zircon solubility on SiO_2 and peraluminosity of the melt. To determine a range of possible variations of Zr partition coefficient (D_{Zr}) between zircon and coexisting melt, we used major element compositions of colorless, pale and brown interstitial glasses and their respective Zr concentrations ranging from ~150 to ~2000 μg/g, but fixed the concentration of Zr in zircon (64.27 ± 1.42 wt% ZrO_2, 2 SD, representing average of eight individual EPMA analyses that corresponds to 475,846 ± 10,514 μg/g Zr). Temperature intervals from ~720 to ~1010 °C and from ~840 to ~1000 °C were obtained for granite and Qz-monzonite-type xenoliths, respectively. In the most cases, the upper ends of the obtained T-intervals match well the temperatures inferred from Opx–Cpx–Mag–Ilm geothermometry (calculated by QUILF), but extending to systematically lower temperatures (Fig. 6a). The granite samples exhibit systematically lower $T_{Zrn\text{-}sat}$ than T calculated by QUILF, except for IC03-130-19, where $T_{Zrn\text{-}sat}$ only barely corresponds to the QUILF range.

The zircon crystallization temperatures ($T_{Zrn\text{-}cryst}$) were calculated using the most recent Ti-in-Zrn thermometer calibrated by Ferry and Watson (2007), which also takes into account activities of SiO_2 and TiO_2 in silicate melt coexisting with zircon. As previously noted by Carley et al. (2011), the activity of SiO_2 in a silicic melt (a_{SiO_2}) is usually >0.5 and its underestimation may lead to significantly lower (by tens of degrees) temperatures. In our Ti-in-Zrn calculations, we used a_{SiO_2} values calculated by QUILF (Table 1). As noted by Hayden and Watson (2007) and Carley et al. (2011), the activity of TiO_2 (a_{TiO_2}) in silicic magmas usually varies from 0.5 to 1.2, with a mean value of ~0.68. However, in order to correctly estimate a_{TiO_2} using the Hayden and Watson (2007) model, saturation of melt with rutile is desirable. Since no rutile was detected in the studied here xenoliths, we applied a uniform $a_{TiO_2} = 0.7$ throughout all T calculations, similar as done by Carley et al. (2011). The obtained T-intervals are much wider

Table 1 Temperature and oxygen fugacity

Sample *N* Rock type Note	Phases	IC03-130-02 Oz-mnzt Range	Avg. ± 2σ	IC03-130-15 Oz-mnzt Range	Avg. ± 2σ	IC03-130-16 Oz-mnzt Range	Avg. ± 2σ	IC03-130-17 Oz-mnzt Range	Avg. ± 2σσ
Temperature, QUILF[(a)]									
a_{SiO_2}		0.83–0.99	0.91 ± 0.09	0.94–1	0.99 ± 0.04	0.84–0.94	0.90 ± 0.08	0.95–1	0.98 ± 0.05
T (°C)	Opx + Cpx + Mag ± Ilm	–	–	–	–	942–1012	970 ± 43	–	–
T (°C)	Opx + Mag ± Ilm	891–936	915 ± 26	–	–	873–979	918 ± 71	–	–
T (°C)	Cpx + Mag ± Ilm	–	–	883–948	912 ± 39	940–1006	969 ± 49	954–1019	981 ± 41
T (°C)	WA	891–936	915 ± 26	883–948	912 ± 39	927–978	952 ± 38	954–1019	981 ± 41
Temperature, Zrn saturation[(b)]									
Zr (μg/g)	Int–Gl	503–1027	807 ± 378	1567–1907	1728 ± 257	496–1295	830 ± 774	574–1813	1384 ± 771
ln D_{Zr}		6.14–6.85	6.41 ± 0.51	5.52–5.72	5.62 ± 0.15	5.91–6.87	6.44 ± 0.93	5.57–6.72	5.89 ± 0.71
M		1.39–1.48	1.44 ± 0.05	1.76–1.80	1.78 ± 0.03	1.63–1.69	1.67 ± 0.04	1.68–1.81	1.78 ± 0.08
$T_{Zrn\text{-}sat}$ (°C)		871–974	931 ± 70	975–1002	990 ± 21	836–961	892 ± 122	851–993	951 ± 87
Temperature, Ti-in-Zrn[(c)]									
Ti (μg/g)	Zrn	5.4–56.6	20 ± 36	4.7–44.8	14 ± 23	3–82.8	15 ± 39	5.4–65.7	15 ± 31
$T_{Zrn\text{-}cryst}$ (°C)		714–976	810 ± 196	709–955	792 ± 142	665–1030	769 ± 201	720–1008	794 ± 163
Oxygen fugacity, QUILF[a]									
log f_{O_2} (atm.)	Opx + Cpx + Mag ± Ilm	–	–	–	–	–10.7 to –9.9	–10.3 ± 0.5	–	–
ΔFMQ		–	–	–	–	1.3–1.5	1.4 ± 0.1	–	–
log f_{O_2} (atm.)	Opx + Mag ± Ilm	–11 to –10.1	–10.6 ± 0.5	–	–	–11.4 to –10.1	–10.8 ± 0.9	–	–
ΔFMQ		1.7–2.8	1.9 ± 0.6	–	–	1.4–1.9	1.6 ± 0.3	–	–
log f_{O_2} (atm.)	Cpx + Mag ± Ilm	–	–	–11 to –10.5	–10.7 ± 0.3	–10.8 to –10	–10.3 ± 0.5	–10.6 to –9.6	–10.1 ± 0.6
ΔFMQ		–	–	1.6–2.1	1.9 ± 0.3	1–1.7	1.3 ± 0.4	1.2–1.5	1.4 ± 0.2
log f_{O_2} (atm.)	WA	–11 to –10.1	–10.6 ± 0.5	–11 to –10.5	–10.7 ± 0.3	–10.8 to –10.1	–10.4 ± 0.6	–10.6 to –9.6	–10.1 ± 0.6
ΔFMQ		1.7–2.8	1.9 ± 0.6	1.6–2.1	1.9 ± 0.3	1.3–1.5	1.4 ± 0.1	1.2–1.5	1.4 ± 0.2

Sample *N* Rock type Note	Phases	IC03-130-14 Granite Range	Avg. ± 2σ	IC03-130-18 Granite Range	Avg. ± 2σ	IC03-130-19 Granite Range	Avg. ± 2σ
Temperature, QUILF							
a_{SiO_2}		0.98–1	0.99 ± 0.01	1	1 ± 0	0.98–1	0.99 ± 0.01
T (°C)	Opx + Cpx + Mag ± Ilm	1093–1177	1128 ± 52	–	–	–	–
T (°C)	Opx + Mag ± Ilm	984–1105	1032 ± 77	1024–1205	1146 ± 128	888–1007	929 ± 78
T (°C)	Cpx + Mag ± Ilm	1103–1197	1136 ± 54	–	–	–	–
T (°C)	WA	1070–1148	1106 ± 52	1024–1205	1146 ± 128	888–1007	929 ± 78

Table 1 continued

Sample *N* Rock type Note	Phases	IC03-130-14 Granite Range	Avg. ± 2σ	IC03-130-18 Granite Range	Avg. ± 2σ	IC03-130-19 Granite Range	Avg. ± 2σ
Temperature, Zrn saturation							
Zr (μg/g)	Int–Gl	493–1997	1528 ± 1195	183–642	387 ± 329	148–1130	631 ± 725
ln D_{Zr}		5.47–6.87	5.84 ± 1.1	6.61–7.86	7.20 ± 0.91	6.04–8.07	6.81 ± 1.47
M		1.67–1.81	1.76 ± 0.1	1.42–1.49	1.45 ± 0.05	1.57–1.68	1.62 ± 0.08
$T_{Zrn\text{-}sat}$ (°C)		834–1011	963 ± 140	755–900	828 ± 104	717–943	855 ± 168
Temperature, Ti-in-Zrn							
Ti (μg/g)	Zrn	–	–	–	–	–	–
$T_{Zrn\text{-}cryst}$ (°C)		–	–	–	–	–	–
Oxygen fugacity, QUILF							
log f_{O_2} (atm.)	Opx + Cpx + Mag ± Ilm	–7.7 to –6.9	–7.4 ± 0.6	–	–	–	–
ΔFMQ		1.8–2.2	2.0 ± 0.3	–	–	–	–
log f_{O_2} (atm.)	Opx + Mag ± Ilm	–8.9 to –7.5	–8.3 ± 0.9	–8.4 to –5.9	–6.7 ± 1.7	–9.9 to –8.2	–9.3 ± 1.1
ΔFMQ		2.1–2.6	2.4 ± 0.3	1.9–2.6	2.4 ± 0.5	2.7–3.1	2.9 ± 0.2
log f_{O_2} (atm.)	Cpx + Mag ± Ilm	–7.8 to –6.8	–7.3 ± 0.6	–	–	–	–
ΔFMQ		1.6–2.2	1.9 ± 0.3	–	–	–	–
log f_{O_2} (atm.)	WA	–8.0 to –7.1	–7.6 ± 0.7	–8.4 to –5.9	–6.7 ± 1.7	–9.9 to –8.2	–9.3 ± 1.1
ΔFMQ		1.8–2.3	2.0 ± 0.2	1.9–2.6	2.4 ± 0.5	2.7–3.1	2.9 ± 0.2

(a) The geothermometers and oxygen barometers used in calculation are models of Andersen and Lindsley (1988) and Frost et al. (1988) realized in the QUILF program (Andersen et al. 1993); a_{SiO_2} is activity of SiO_2 calculated as mole fraction of SiO_2 in coexisting interstitial glass (see text); Opx = orthopyroxene, Cpx = clinopyroxene, Mag = magnetite, Ilm = ilmenite are mineral associations used for calculation of temperature (T °C) and oxygen fugacity (log f_{O_2} atm.) for 1 atm. total pressure; ΔFMQ is deviation from FMQ oxygen fugacity buffer at a given temperature and defined as $(\log f_{O_2})_{sample} - (\log f_{O_2})_{FMQ}$. The listed T and f_{O_2} values represent ranges (Range) and averages of several calculations given at 2σ standard deviation (Avg. ± 2σ), where the compositions of analyzed ilmenites cross-referenced with Opx + Cpx + Mag, Opx + Mag and Cpx + Mag associations were used. Afterwards, the respective weighted average values (WA) were calculated and accepted as true and representative for a given sample

(b) Zircon saturation temperature ($T_{Zrn\text{-}sat}$ °C) was calculated using the revised equation of the zircon solution model (Boehnke et al. 2013), ln D_{Zr} is the ratio of Zr concentration in zircon (always kept constant during calculations at 475,846 μg/g) to that in the melt; M is a compositional factor ("melt basicity") that accounts for dependence of zircon solubility on SiO_2 and peraluminosity of the melt (= [Na + K + 2Ca]/[Al*Si]) (Watson and Harrison 1983)

(c) Temperature of zircon crystallization and growth ($T_{Zrn\text{-}cryst}$ °C) was calculated using the most recent Ti-in-Zrn thermometer equation calibrated by Ferry and Watson (2007)

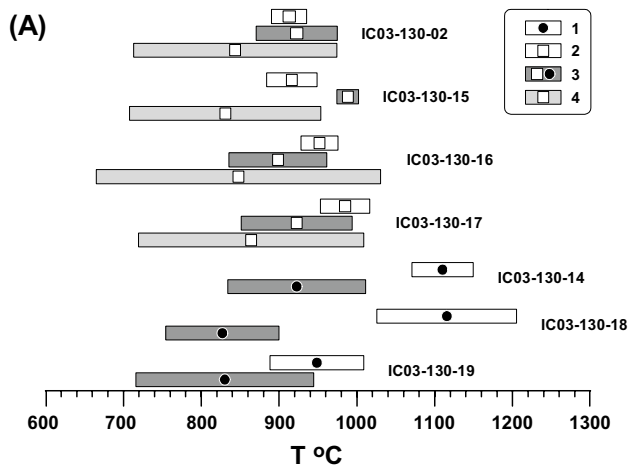

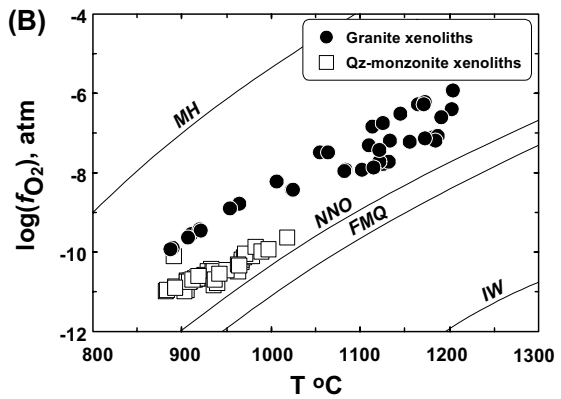

Fig. 6 Temperature and oxygen fugacity conditions in the magma chamber. **a** Temperature of Opx–Cpx equilibrium calculated by QUILF of granite (*1*) and Qz-monzonite (*2*) xenolith types given in comparison with temperatures of zircon saturation (*3*) and of zircon saturation and growth (*4*)

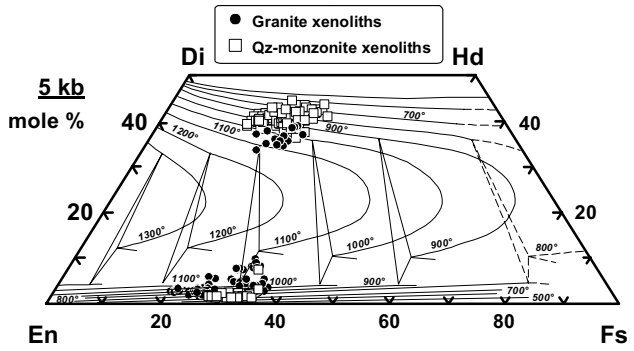

Fig. 7 Wo–En–Fs triangular diagram of pyroxene composition with isotherms corresponding to the 5 kbar experiments of Lindsley (1983)

(broad range 665–1030 °C; Fig. 6a) than the temperatures of melt saturation with Zrn. The upper ends of the Ti-in-Zrn *T*-ranges are consistent with those calculated by QUILF.

U–Pb zircon geochronology

Total 91 zircons, 12–17 grains from each of 6 samples, most of them studied for O isotopes, were provisionally analyzed in October 2009 using the NENIMF CAMECA IMS 1280 ion microprobe (Woods Hole Oceanographic Institution, USA) and then, in June 2012, they were repeatedly dated using the CAMECA IMS 1270 instrument at the University of California Los Angeles (UCLA). The analytical conditions (see *Supporting Online Material*) were similar for both laboratories. Also, a subset of the "youngest" zircons (9 grains, 2–3 from 4 of 6 samples) was repeatedly dated at UCLA in continuation of the June 2012 session by U–Th geochronology method. The technique details are given in Schmitt et al. (2003, 2006) (for more information, see *Supporting Online Material*). The zircons were corrected for common Pb, assuming concordance of the studied zircons. We think that this assumption is justified because no inherited grains and/or overgrown zircon cores but mostly regular zoning were identified. We used a correction method based on the Getty and DePaolo (1995) approach. Since common Pb is believed to come dominantly from sample surface (Schmitt et al. 2003 and references therein), we consequently utilized an anthropogenic common $^{207}Pb/^{206}Pb$ ratio ($R_c^{7/6}$) of 0.8283 (Sañudo-Wilhelmy and Flegal 1994) using *Isoplot 3.70* (Ludwig 2008).

Figure 8 presents Terra–Wasserburg Concordia diagrams for individual zircons showing ages (uncorrected for Th/U partition between coexisting zircons and silicate melts) of six studied crustal xenoliths (Table 2; individual zircon analyses are given in Table B7, *Supporting Online Material*). All zircons appeared to be relatively young (0.1–0.19 Ma) and require strong correction for common Pb (~80 % in average and up to 99 % in the most extreme cases). The U–Pb zircon ages approximate a normal distribution for each individual sample (insets in Fig. 8 showing cumulative probability curves calculated using *Isoplot 3.70*), suggesting that each individual xenolith contains zircons of a common population. High proportion of the common Pb results in high uncertainty (about ±0.17 Ma, 2 SE) for individual zircons, thereby precluding precise single-grain dating. Consequently, our age determinations represent weighted averages for the entire zircon population from each individual sample estimated with the uncertainty of ±0.022–0.045 Ma, 2 SE.

The concentrations of U (58–690 μg/g) and Th (4–508 μg/g), and Th/U ratios (0.31 ± 0.20, 2 SD) are in the range of igneous zircons (Th/U ~0.2 to ~0.9; Hoskin and Schaltegger 2003; Bindeman et al. 2006). After correcting for initial U–Th disequilibrium (Schärer 1984; Schmitt et al. 2003), taking into account Th/U ratios of individual zircons

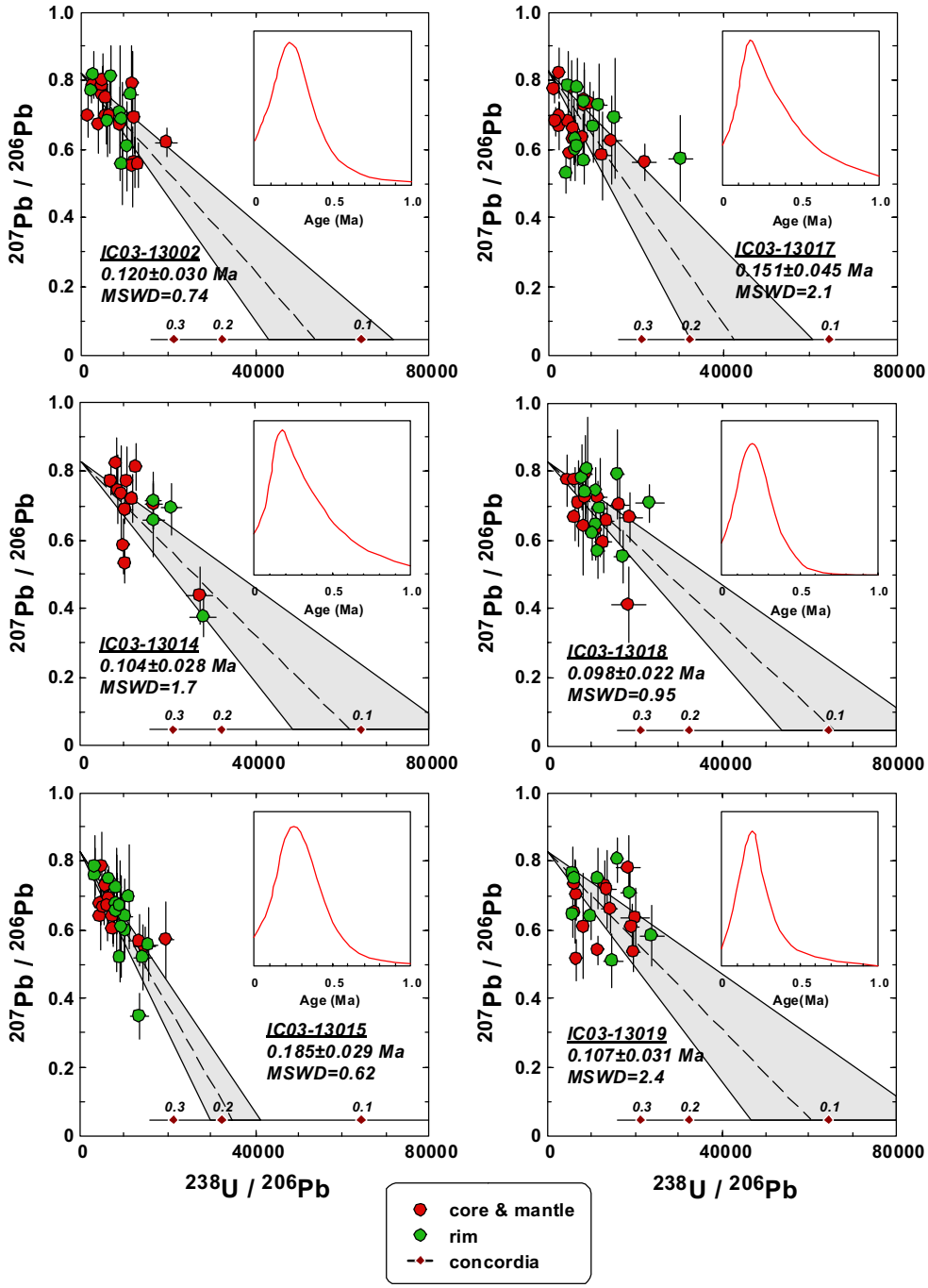

Fig. 8 Terra–Wasserburg Concordia diagrams for individual zircons showing error-weighted ages (uncorrected for Th/U partition between coexisting zircons and silicate melts). A fixed $^{207}Pb/^{206}Pb = 0.8283$ (Sañudo-Wilhelmy and Flegal 1994) was used to determine the intercept with Concordia. The *insets* show cumulative probability curves of the obtained zircon ages. *Error bars* of individual zircons are shown at $\pm 1\sigma$ level, the uncertainty of the obtained ages are given at 95 % confidence level

(Table B7, *Supporting Online Material*) and average Th/U ratios of coexisting interstitial glasses, the U–Th disequilibrium corrected U–Pb isochron ages were obtained to be 0.2–0.27 Ma (Table 2). Considering total 144 dated zircons as a single population, the average age of 0.212 ± 0.010 Ma, MSWD = 0.41 was finally acquired.

The young U–Pb age was additionally confirmed by the U–Th geochronology method. The selected 9 zircon grains from four samples (15 individual analyses; Table 3) deviate from secular equilibrium with regard to $^{230}Th/^{238}U$ and fall below the equiline in Fig. 9. Disequilibrium ages were calculated by regression through all data points (counting

Table 2 Summary of U–Pb zircon dating results

Sample *N*	Grains	Spots	U (μg/g)	±1σ	Th (μg/g)	±1σ	$(Th/U)_{Zrn}$	±1σ	$^{238}U/^{206}Pb$ *Uncorrected ratios*	±1σ	MSWD	$^{207}Pb/^{206}Pb$	±1σ	MSWD
Qz-monzonite xenoliths														
IC03-130-2	17	24	190	124	58	36	0.31	0.08	4088	590	23.4	0.708	0.018	1.4
IC03-130-15	17	28	184	112	63	61	0.34	0.11	5689	582	12.6	0.647	0.019	1.8
IC03-130-17	15	29	171	99	63	67	0.37	0.11	2369	372	29.3	0.676	0.014	1.3
Granite xenoliths														
IC03-130-14	12	16	297	132	97	64	0.33	0.07	10,819	1059	8.9	0.662	0.035	4.3
IC03-130-18	16	25	266	88	81	37	0.30	0.05	7529	697	11.5	0.694	0.015	1.1
IC03-130-19	14	22	312	157	116	107	0.37	0.14	8237	839	17.1	0.652	0.020	1.9

	$^{206}Pb_c$ [(a)] (%)	±1σ	Age [(b)] (Ma)	±2σ	MSWD	$(Th/U)_{Mlt}$	$^{238}U/^{206}Pb$ *Disequilibrium corrected* [(c)]	±1σ	MSWD	Age [(d)] (Ma)	±2σ	MSWD
Qz-monzonite xenoliths												
IC03-130-2	83	11	0.120	0.030	0.74	3.68	22,953	1332	0.29	0.23	0.02	0.24
IC03-130-15	76	12	0.185	0.029	0.62	3.91	20,941	887	0.23	0.27	0.02	0.22
IC03-130-17	80	10	0.151	0.045	2.1	2.71	14,988	1572	0.93	0.21	0.04	0.66
Granite xenoliths												
IC03-130-14	80	17	0.104	0.028	1.7	4.34	27,756	1596	0.43	0.20	0.02	0.46
IC03-130-18	82	12	0.098	0.022	0.95	4.48	26,846	1229	0.23	0.20	0.02	0.30
IC03-130-19	79	11	0.107	0.031	2.4	4.82	24,414	1809	0.91	0.20	0.03	0.69

Individual zircon analyses are given in Table B7, *Supporting Online Material*

(a) Common Pb obtained using Y intercept in the $^{238}U/^{206}Pb$ versus $^{207}Pb/^{206}Pb$ diagram fixed at $^{207}Pb/^{206}Pb$ ($R_c^{7/6}$) of 0.8283 (anthropogenic common $^{207}Pb/^{206}Pb$ ratio; Sañudo-Wilhelmy and Flegal 1994)

(b) Concordia intercept age inferred from $^{238}U/^{206}Pb$ ratios uncorrected for the effect of the initial ^{230}Th disequilibrium (Schärer 1984) using *Isoplot 3.70* (Ludwig 2008)

(c) $^{238}U/^{206}Pb$ ratios were corrected for the initial U–Th disequilibrium as described by Schmitt et al. (2003). The zircon-melt distribution coefficients ($D^{Th/U}{}_{Zrn-Mlt}$) were calculated from $[Th/U]_{Zrn}$ ratios of each individual zircon and average $[Th/U]_{Mlt}$ ratio of interstitial glasses of the respective samples (given in $[Th/U]_{Mlt}$ column)

(d) Accepted $^{206}Pb_c$ and U–Th disequilibrium corrected age

Table 3 U–Th zircon dating results

Sample note	Spot	$^{238}U/^{232}Th$	$\pm 1\sigma$	$^{230}Th/^{232}Th$	$\pm 1\sigma$	U (μg/g)
IC03-130-2, Qz-monzonite						
130-02-zrn3c	Core	5.23	0.03	4.55	0.23	212
130-02-zrn3r	Rim	4.85	0.04	3.97	0.24	261
130-02-zrn5c	Core	5.33	0.03	4.73	0.31	151
130-02-zrn5r	Rim	7.11	0.04	5.51	0.55	134
IC03-130-15, Qz-monzonite						
130-15-zrn5r	Rim	5.12	0.02	4.52	0.24	191
130-15-zrn9c	Core	3.84	0.04	3.47	0.13	410
130-15-zrn9 m	mantle	5.62	0.03	5.24	0.29	154
130-15-zrn9r	Rim	5.66	0.03	5.34	0.28	172
IC03-130-17, Qz-monzonite						
130-17-zrn1c	Core	5.40	0.04	5.09	0.52	96
130-17-zrn2c	Core	6.55	0.04	5.23	0.45	129
130-17-zrn2r	Rim	4.80	0.02	4.42	0.20	235
130-17-zrn14c	Core	6.05	0.06	5.16	0.29	160
130-17-zrn14r		5.40	0.03	4.73	0.30	169
IC03-130-17, Granite						
130-18-zrn2c	Core	5.52	0.05	4.64	0.19	391
130-18-zrn4c	Core	5.94	0.03	4.93	0.35	166

U–Th disequilibrium ages were calculated by regression through all data points using *Isoplot 3.70* (Ludwig 2008). This yields the age of 0.156 ± 0.073 Ma, MSWD = 0.72 (Fig. 9)

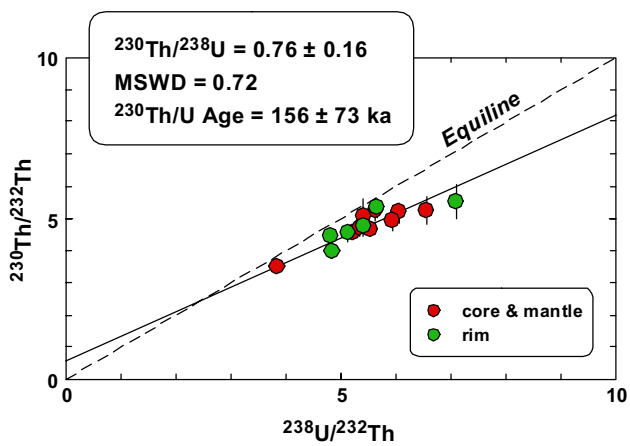

Fig. 9 The $^{230}Th/^{232}Th$ versus $^{238}U/^{232}Th$ isochron diagram for a selected individual zircons from four of seven studied crustal xenoliths. Error-weighted regression was calculated and shown with 2σ uncertainty. *Bars* in individual symbols represent $\pm 2\sigma$ error; if not shown, the size of the symbols exceeds the $\pm 2\sigma$ uncertainty

together zircon cores, mantles and rims) using *Isoplot 3.70* (Ludwig 2008). This yields the age of 0.156 ± 0.073 Ma, MSWD = 0.72.

Oxygen isotopes

Oxygen isotopic compositions (given in permil of $\delta^{18}O$ relative to SMOW) of individual quartz and feldspar grains and associated interstitial glasses, all extracted from ~1 to 3 cm^3 domains of the host xenoliths, were obtained using the single-grain laser fluorination (LF) method at the University of Oregon (Bindeman 2008) with the precision of ~0.1 ‰ (1 SD). A primary Gore Mt. garnet standard (UWG-2, $\delta^{18}O = 5.8$ ‰; Valley et al. 1995) and a secondary Gore Mt. reference garnet (UOG, $\delta^{18}O = 6.52$ ‰) were always run concurrently. Also, a subset of 59 zircon grains from these samples, in which core, mantle and rim zones were systematically analyzed, has been studied using the CRPG-Nancy CAMECA IMS 1270 and IMS 1280 HR instruments, with the precision of 0.2–0.4 ‰ (95 % confidence level) (for more detail, see *Supporting Online Material*). The obtained precisions of the LF and SIMS methods were used as a benchmark in discriminating analytical versus natural intra- and inter-grain variations. The variations of $\delta^{18}O$ in excess of ±0.2 ‰ recorded by LF and in excess of ±0.4 ‰ by SIMS were considered as natural. The results are listed in Table B8 (*Supporting Online Material*). The following important observations can be made based on these data:

1. The transporting hyaloclastites are characterized by "normal", MORB-like to slightly lower $\delta^{18}O$ values of 5.3–5.5 ‰, whereas one spatially associated with them basaltic lava has lower $\delta^{18}O$ of 4.9 ‰. In contrast, strongly varying $\delta^{18}O$ values and systematically ^{18}O-enriched signature have been recorded in the rock-

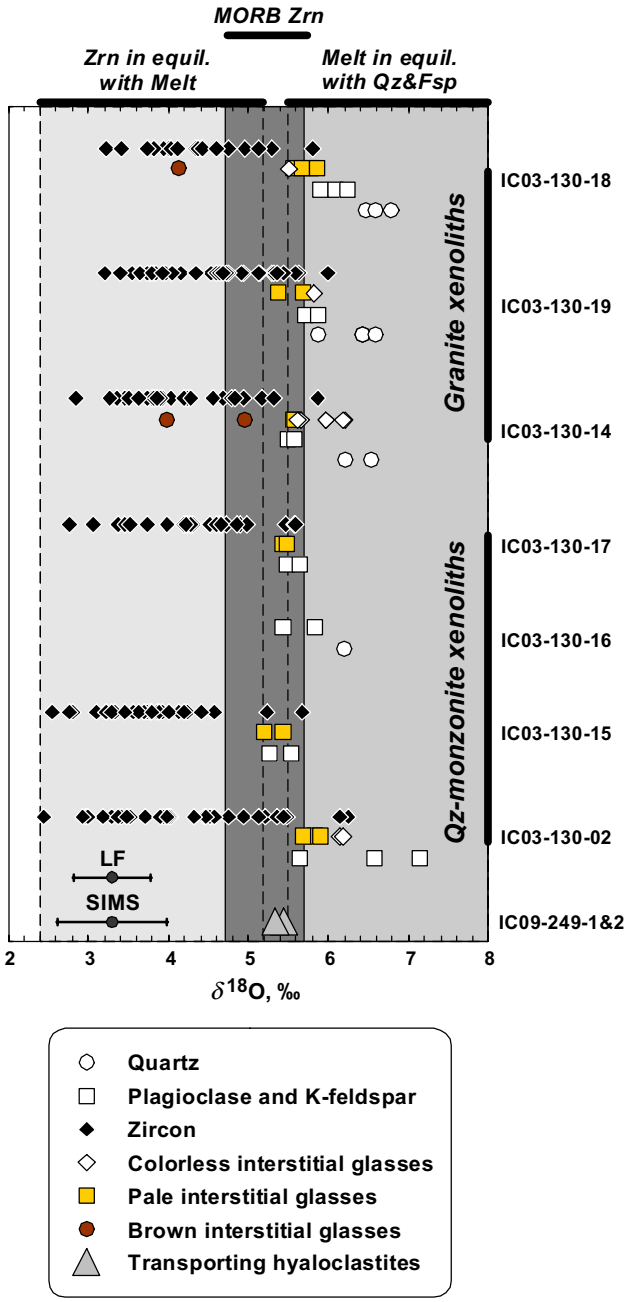

Fig. 10 Oxygen isotope compositions of individual quartz, feldspar and zircon crystals, colorless to brown interstitial glasses and transporting hyaloclastites. The *MORB Zrn shaded dark-gray vertical band* denotes the range of mantle-like $\delta^{18}O_{Zrn}$ values from oceanic plagiogranites and gabbros (5.2 ± 0.5 ‰, Grimes et al. 2011). The *Melt in equil. with Qz&Fsp gray shaded band* denotes the range of silicic melt $\delta^{18}O$ values in equilibrium with analyzed quartz and feldspar crystals, based on the experimental and model calculation data of Chiba et al. (1989), Chacko et al. (2001); Zheng (1991, 1993), Zhao and Zheng (2003). The *Zrn in equil. with Melt light-gray shaded* band denotes the range of $\delta^{18}O_{Zrn}$ values in equilibrium with interstitial glasses, based on the experimental and empirical data on oxygen isotope fractionation factors between Qz-, Zrn- and SiO_2-rich silicate melt taken from Bindeman and Valley (2002, 2003) and Valley et al. (2003). The *LF* and *SIMS error bars* represent the highest ±2σ analytical uncertainty attained for the respective method

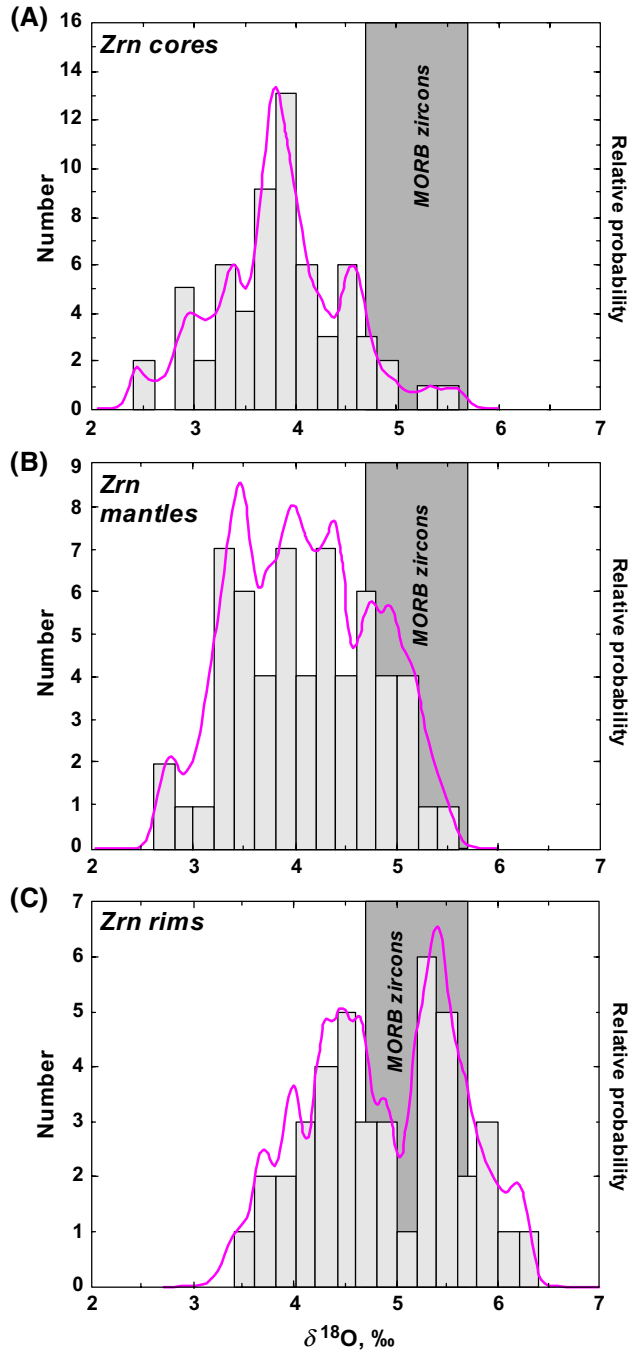

Fig. 11 Oxygen isotope composition ranges of zircon cores (**a**), mantles (**b**) and rims (**c**) from the studied Tindfjöll leucocratic xenoliths. *Curves* show cumulative probability density functions of the $\delta^{18}O$ variations calculated using *Isoplot 3.70* (Ludwig 2008). The *shaded vertical band MORB zircons* denote the range of mantle-like $\delta^{18}O_{Zrn}$ values from oceanic plagiogranites and gabbros (5.2 ± 0.5 ‰, Grimes et al. 2011)

forming silicate minerals of the xenoliths. The widest range of ~4 ‰ was determined in zircons by SIMS and ~2 ‰ in interstitial glasses by LF. Five of 11 analyzed Qz grains from one granite xenolith IC03-130-18

exhibit a range of 5.9–6.6 ‰ that closely corresponds the entire range of $\delta^{18}O$ values (5.9–6.8 ‰) measured in quartz from the other xenoliths. Similar wide range of 5.7–7.2 ‰ was found in feldspars from Qz-monzonite xenolith IC03-130-02.

2. Despite the observed wide $\delta^{18}O$ ranges, spatially associated Qz and Fsp appear to be in high-temperature (800–1200 °C), O-isotope equilibrium with each other and with neighboring colorless (5.5–6.2 ‰, $N = 10$), pale or light brownish (5.1–5.9 ‰, $N = 15$) interstitial glasses (Fig. 10). This follows from oxygen isotope fractionation factors between Qz, Fsp and SiO_2-rich silicate melt (Mlt) calculated for the given above temperature conditions ($\Delta_{Qz-Fsp} = \delta^{18}O_{Qz}–\delta^{18}O_{Fsp} = 0.5–1.0$ ‰, $\Delta_{Qz-Mlt} = \delta^{18}O_{Qz}–\delta^{18}O_{Mlt} = 0.2–0.5$ ‰, and $\Delta_{Fsp-Mlt} = \delta^{18}O_{Fsp}–\delta^{18}O_{Mlt} = -0.3$ to -0.6 ‰, respectively), using experimental data and model calculations of Chiba et al. (1989), Chacko et al. (2001), Zheng (1991, 1993) and Zhao and Zheng (2003). This also implies that no secondary processes have affected the xenoliths after their formation and the residual isotopic inter- and intra-crystal O-isotope heterogeneity is juvenile. Figure 10 demonstrates that the range of calculated $\delta^{18}O_{Mlt}$ values in equilibrium with Qz and Fsp (given that $\Delta_{Qz-Mlt} = 0.3 \pm 0.1$ ‰ and $\Delta_{Fsp-Mlt} = -0.5 \pm 0.3$ ‰ at $T = 800–1200$ °C) spans from 5.5 to as high as 8 ‰, covering almost the entire range of $\delta^{18}O$ observed in the colorless to light brownish interstitial glasses (except for two pale glasses with $\delta^{18}O = 5.2$ and 5.4 ‰).
3. The dark-brown to black interstitial glasses (with $\delta^{18}O$ ranging from 4.0 to 5.0 ‰, $N = 3$) are out of oxygen isotope equilibrium with Qz and Fsp, as follows from the computed $\delta^{18}O_{Mlt}$ values (Fig. 10). Two explanations can be suggested. First, black mingling glass (as from IC03-130-14; Fig. 3a–c) may represent relicts of a more mafic, hybrid melt resulting from interaction of silicic crustal rocks with a hotter, primitive basaltic magma. This could happen during progressive partial melting of already solidified silicic rocks caused by their heating in the vicinity of hot fissure swarm (Gunnarsson et al. 1998). The intruding magma might have relatively low $\delta^{18}O$ values (similar to the basalt lava associated with the transporting hyaloclastites), but being out of O-isotope equilibrium with the surrounding silicic rocks. Dark-colored glasses may thus represent quenched, non-homogenized relicts of the latter hybrid magma. Second, the observed $\delta^{18}O$ values of the dark-brown glasses could result from dissolution of magnetite ± zircon intra-grain clumps, also due to interaction of the solid rock with hot magma because magnetite has always lower $\delta^{18}O$ than coexisting silicate melt ($\Delta^{18}O_{Mag-Mlt} = \delta^{18}O_{Mag}–\delta^{18}O_{Mlt} = -2.7$ to -5.0 ‰ at T = 800–1200 °C). We think that both possibilities are plausible.
4. Zircons extracted from individual xenoliths are strongly heterogeneous in oxygen isotope composition. They show a broad range of $\delta^{18}O$ from 2.4 to 6.3 ‰, without significant difference between the granite and Qz-monzonite xenolith types (Fig. 11). Oxygen isotope compositions obtained in zircon cores (2.4–5.6 ‰, average 3.9 ± 1.3 ‰, 2 SD), mantles (2.8–5.5 ‰, average 4.1 ± 1.4 ‰, 2 SD) and rims (3.4–6.3 %, average 4.9 ± 1.5 ‰, 2 SD) overlap each other. However, their $\delta^{18}O$ values are not equally distributed. The probability density distribution curves reveal a maximum at $\delta^{18}O$ of ~3.8 ‰ of Zrn cores (Fig. 11a), four less pronounced peaks between ~3.5 and 4.9 ‰ of Zrn mantles (Fig. 11b) and two clear populations at ~4.5 and ~5.5 ‰ of Zrn rims (Fig. 11c).
5. The expected $\delta^{18}O$ values of zircons in equilibrium with black through colorless interstitial glasses range from 2.4 to 5.2 ‰ (Fig. 10). This range has been computed using the existing experimental and empirical data on O-isotope fractionation factors between Qz, Zrn and SiO_2-rich silicate melts ($\Delta_{Zrn-Mlt} = \delta^{18}O_{Zrn}–\delta^{18}O_{Mlt} = -1.4 \pm 0.4$ ‰ at $T = 800–1200$ °C; Bindeman and Valley 2002, 2003; Valley et al. 2003). The calculated range almost entirely corresponds to the measured $\delta^{18}O_{Zrn}$ values. Only a minor population of Zrn from the lower end of the spectrum maintains equilibrium with black and dark-brown glasses. This implies that the majority of zircons with higher $\delta^{18}O_{Zrn}$ values could crystallize from colorless, pale or light brown interstitial melts because of the high Zr concentrations (up to 2000 μg/g), suggesting overall saturation of the melt with zircon.
6. The Zrn rims with $\delta^{18}O_{Zrn} = 5.7–6.3$ ‰ are out of the range of MORB zircons. Since the difference is larger than the attained 2σ uncertainty of SIMS (±0.4 ‰), this suggests crystallization of these Zrn rims from a melt with $\delta^{18}O$ of as high as 8 ‰, in agreement with the calculated $\delta^{18}O_{Mlt}$ values in equilibrium with Qz and Fsp.

Discussion

Zircon growth, recycling and inheritance

Generally, calculated temperature of zircon saturation represents a lower limit, if magma was undersaturated with zircon and a maximum estimation, if it was saturated (Watson and Harrison 1983; Miller et al. 2003). The upper end of the $T_{Zrn-sat}$ range obtained during the present study (~720–1010 °C) is similar and only by ~70 °C lower (in

sample IC03-130-16) than the temperature of Zrn crystallization ($T_{Zrn\text{-}cryst}$ broad range ~670–1030 °C) (Fig. 6a). Also, the $T_{Zrn\text{-}sat}$ ranges are much narrower than those of $T_{Zrn\text{-}cryst}$, being similar to ~60 °C higher than the temperatures obtained for zircons from the Askja, Hekla, Öræfajökull and Torfajökull silicic eruptions (~700–950 °C; Gunnarsson et al. 1998; Carley et al. 2011). The temperature calculated by QUILF ($T_{QUILF} \approx$ 880–1205 °C) is thought to reflect that of the last equilibrium of xenolith-forming minerals with interstitial melt shortly prior to eruption. It is very similar to $T_{Zrn\text{-}sat}$ obtained for zircons hosted in Qz-monzonite xenoliths, implying that the reacting melt was always Zrn-saturated, while interacting with the host silicic rock. In contrast, two of three granite xenoliths exhibit a significant gap (by ~60 to more than 100 °C) between $T_{Zrn\text{-}sat}$ and T_{QUILF} (Fig. 6a), suggesting that these zircons were formed at lower temperature from more evolved and Zrn-saturated silicic melts.

Abundant zircons having euhedral shape and simple zoning in all studied samples, calculated relatively high temperatures of Zrn saturation and high concentrations of Zr in the melt imply immediate, intra-grain crystallization of at least the majority of zircons from a hybrid melt. These zircons could be then accumulated in a crystal mush layer of a magma chamber. In this context, all studied xenoliths likely represent disintegrated, partially melted crystallization products of the same or chemically similar, ~0.2–0.25 My old silicic magmas, which were probably resulted from precursor crustal anatexis events.

On the other hand, each individual xenolith contains a subordinate amount of zircons, which has crystallized at temperatures either higher or lower than $T_{Zrn\text{-}sat}$ (Fig. 6a), suggesting their inheritance. Indeed, if $T_{Zrn\text{-}cryst}$ is higher than $T_{Zrn\text{-}sat}$, this is usually interpreted as entrainment of already formed zircons in a second, possibly compositionally distinct, Zrn-undersaturated magma (e.g., Miller et al. 2003; Carley et al. 2011; Harrison et al. 2007). The inherited zircons would be preserved over time at metastable conditions in the magma, and as noted by Miller et al. (2003), their saturation temperatures are thus meaningless. Although large zircons (>90 μm size) can be dissolved in Zrn-undersaturated magmas at ~800 °C during a few thousand years, their encapsulation between larger grains (similar to the Mag ± Ilm segregations with adhering Zrn surrounded by large Fsp and Qz grains; Fig. 3) would protect them from rapid dissolution, explaining the observed discrepancy between $T_{Zrn\text{-}sat}$ and $T_{Zrn\text{-}cryst}$ (Watson 1996).

Oxygen fugacity

Gunnarsson et al. (1998) have shown that crystallization of the Torfajökull rhyolites occurred at oxygen fugacity conditions close to, or ~0.5 log units below, FMQ buffer. Schattel et al. (2014) have demonstrated, however, that redox state of the Icelandic rhyolites from different locations is not uniform. For example, Hekla (ΔFMQ of–0.9 ± 0.2 log atm.) and off-rift Öræfajökull rhyolites (ΔFMQ from–0.4 to–0.1 ± 0.2 log atm.) are predominantly reduced, whereas a pumice from Askja is more oxidized (ΔFMQ = 1.4 ± 0.1 log atm.). Schattel et al. (2014) have noted also that ΔFMQ values and oxygen isotope composition of minerals and glasses from these lavas vary coherently and appear to be strongly different for the rift and off-rift volcanic systems. Thus, more oxidized rift-related tephra from Askja have low $\delta^{18}O$ of ~1.3 ‰, reflecting assimilation of hydrothermally altered, more oxidized shallow crust, whereas off-rift magmas from Öræfajökull are reduced and show "normal" to slightly lowered $\delta^{18}O$ values of 5.2–6 ‰, suggesting no or minor contamination by crustal rocks.

We demonstrate that the interstitial melts from the studied xenoliths, especially those in the granite type, were formed at rather oxidized conditions (ΔFMQ from 1.2 to 3.1; Fig. 6b), in agreement with the observations by Schattel et al. (2014). It is worth emphasizing also that Tindfjöll is situated in the currently active rift zone. We ascribe such oxidized conditions to near-surface hydrothermal metamorphism caused by meteoric and probably marine waters, as it also follows from our new oxygen isotope data (see discussion below).

Oxygen isotope constraints

Most of the lavas erupted on Iceland are characterized by systematically lower $\delta^{18}O$ values compared to the Earth's mantle, attributed to their derivation from, or interaction with, hydrothermally altered upper-crustal rocks (e.g., Muehlenbachs et al. 1974; Hattori and Muehlenbachs 1982; Condomines et al. 1983; Gautason and Muehlenbachs 1998). Most of the oceanic crustal rocks altered by seawater span over a ~10 ‰ range of $\delta^{18}O$ values (from ~2–3 ‰ to ~11–13 ‰; e.g., Alt et al. 1986; Grimes et al. 2011), spreading on both sides of the "normal"-$\delta^{18}O$ MORB magma value of ~5.6 ± 0.2 ‰. The submarine oceanic crust is high in $\delta^{18}O$ (~6–9 ‰) in its upper level (pillow basalts, sheet dike complexes) due to intensive O-isotope exchange with seawater and consequent leaching ^{18}O isotope from the rocks during low-T (<300 °C) hydrothermal circulations. It is never altered to $\delta^{18}O$ values of as low as ~2–4 ‰ in its middle and lower parts because $\Delta^{18}O_{Rock\text{–}Water}$ isotope fractionation is effectively 0 ± 1 ‰ at high (>500 °C) temperature (Gregory and Taylor 1981; Stakes and Taylor 1992). In contrast, the Icelandic crust is remarkably lower in $\delta^{18}O$ than typical MORB-like oceanic crust (as low as −11 ‰; e.g., Bindeman et al. 2012 and references therein). Thus, secondary fusion or assimilation of such $\delta^{18}O$-low rocks may produce SiO_2-rich magmas with

much larger O-isotope variations than melting of the oceanic crust.

Zircons from typical oceanic crust plagiogranites and gabbros are characterized by remarkably uniform $\delta^{18}O$ values of 5.2 ± 0.5 ‰, being in equilibrium with unaltered MORB ($\delta^{18}O$ of 5.6–5.7 ‰) at high magmatic temperatures (Valley et al. 2005; Grimes et al. 2011). In contrast, zircons from four well-known large-volume silicic units in Iceland (Askja, Hekla, Torfajökull central volcanoes and Austurhorn silicic intrusion) exhibit strong isotope diversity and disequilibria with their transporting magmas (Bindeman et al. 2012; Schattel et al. 2014) and are 1^3 to 10^5 years older than their host rhyolites (for example, the 1875 AD eruption of Askja, the 1158 AD eruption of Hekla; Carley et al. 2011). This suggests that the zircons were carried by different, generally low in $\delta^{18}O$ magma batches, which in turn could derive from hydrothermally altered crustal rocks of different age.

The majority of the studied zircon cores and mantles are systematically lower in $\delta^{18}O$ by 1–2 ‰ than zircons from typical oceanic lithosphere (Fig. 11a, b). On the other hand, there is an increasing number of zircons in the sequence from Zrn cores through their mantles to rims corresponding to the "normal," MORB-like $\delta^{18}O_{Zrn}$ range. This observation and the presence of two $\delta^{18}O$-distinct groups of zircon rims (Fig. 11c) may suggest that we are dealing with at least two populations of zircons having different crystallization history. The first maximum corresponding to $\delta^{18}O$ of ~4.5 ‰ of the Zrn rims, also similar to the $\delta^{18}O$ values of Zrn cores and mantles, may represent an in situ crystallized population of cognate zircons formed under local isotopic equilibrium from "minute" partial melts, yet represented by colorless through pale to dark-brown interstitial glasses. Those Zrn mantles and rims with $\delta^{18}O \leq 5.5$ ‰ may also reflect latter interaction with newer portions of hotter, $\delta^{18}O$-depleted magmas entering magma chamber, being consistent with the observed ultimately lower temperatures of Zrn saturation and growth and systematically higher temperatures of the latter processes of magma–rock interaction fingerprinted in Cpx and Opx (*T* calculated by QUILF).

Five of the studied zircons have rims with $\delta^{18}O$ of 5.8–6.3 ‰, exceed the upper end of the MORB-like zircon range, being out of equilibrium with any of the analyzed interstitial glasses (Figs. 10, 11) and require crystallization from a melt with $\delta^{18}O$ value of as high as 8 ‰. This is in agreement with the calculated $\delta^{18}O_{Mlt}$ values in equilibrium with high-$\delta^{18}O$ Qz and Fsp, which seem to be coeval with the zircon rims. Such elevated $\delta^{18}O$ values are unlikely to produce by interaction of normal-$\delta^{18}O$ (about 5–6 ‰) crustal rocks with low-$\delta^{18}O$ (about–10 ‰) meteoric waters because very high O-isotope fractionation factor ($\Delta^{18}O_{Rock-Water} > 15$ ‰) is required. Such high $\Delta^{18}O_{Rock-Water}$ values can only be attained at very low temperatures (below ~50–70 °C), at which oxygen isotope exchange is sluggish. We thus conclude that the recorded high-$\delta^{18}O$ zircon rims reflect melting of rocks preferentially altered by seawater, rather than extremely low-*T* isotopic exchange with meteoric waters.

Implications for the magma chamber processes

The occurrence of partially melted leucocratic xenoliths provides persuasive evidence that crustal anatexis had an important role in the origin of the Icelandic rhyolites. However, oxygen isotope data of Muehlenbachs et al. (1974) together with the analysis of major elements have lead Sigurdsson and Sparks (1981) to the conclusion that simple partial melting model alone does not explain the origin of the Icelandic rhyolites in full. A complex mechanism including partial or complete fusion of previously formed silicic crustal rocks, hybridization with basaltic magma and subsequent fractional crystallization has been suggested.

Regardless of whether the studied xenoliths are (a) fused relicts of the Icelandic crust "plagiogranites," the products of the earlier partial melting of the older basic rocks (amphibolites) in the presence of H_2O (Sigurdsson 1977); (b) relicts of the subsided evolved intrusives and extrusives located beneath a core of a large central volcano (Gunnarsson et al. 1998) and/or (c) partially melted crystal segregations from the upper parts of solidifying basaltic intrusions (Marsh et al. 1991), they all are thought to reflect the earlier stages of melting of the Icelandic crust. Our new single-grain laser fluorination and ion microprobe data documenting the significant oxygen isotope diversity of zircons and, in lesser extent, of other rock-forming minerals and interstitial glasses ultimately suggest that this partial melting phenomena encompassed diverse in $\delta^{18}O$ crustal rocks and occurred ~0.15–0.25 My ago. These age estimations correspond to the "second last glacial stage" on Iceland, when the majority of subglacial hyaloclastite ridges were formed in the Tindfjöll area (~130–170 ka; e.g., Bourgeois et al. 1998). This implies a relatively short (to about a hundred thousand ± a few tens of thousand years, according to our uncertainty) spatial interval between melting of the anticipated hydrothermally altered Icelandic crust, consequent magma–rock interaction, crystallization and possible inheritance of zircons and final ejection of xenolith-bearing hyaloclastites. Similarly, a relatively short interval (<50 ky) between crystallization of a major part of zircon population and eruption of magma is very common in Iceland and was previously documented for the Askja, Hekla, Öræfajökull and Torfajökull central volcanoes (Carley et al. 2011).

Finally, the "normal," MORB-like to significantly higher $\delta^{18}O$ values of the majority of mineral phases composing the nodules and the associated interstitial glasses likely suggest that the lower Icelandic crust may have been not

globally subjected to low-temperature alteration by meteoric water, at variance with the shallower upper-crust portions composed of basaltic lavas and hyaloclastites (Bindeman et al. 2008). We speculate that the presence of remarkably more positive $\delta^{18}O$ values (>5.6 ‰) found in the coexisting quartz, feldspar and colorless interstitial glass may suggest that the crust beneath the Tindfjöll area could be in contact with seawater during sometime in the past, further back time than the zircon crystallization age. Such processes must result in higher, not lower, than normal MORB $\delta^{18}O$ values in the preconditioned crustal rocks (Taylor and Sheppard 1986). If the volcanic zone, in which the Tindfjöll volcano is located, is ~4 My old (Palmason and Saemundsson 1974; Jakobsson 1979 and references therein) and the latter glacier load has caused an inflow of seawater, then it would argue for partial melting of earlier crystallization products from the same volcano, the interpretation proposed by Gunnarsson et al. (1998), rather than remelting of earlier-formed MORB-like plagiogranites (Sigurdsson 1977). The parental rocks for the Icelandic rhyolites would be then more likely of transitional to alkaline composition but tholeiitic metabasalts that is also in agreement with the overall enriched trace element composition of the studied xenoliths.

Acknowledgments We are very grateful to A.V. Sobolev, K.P. Jochum, B. Stoll and U. Weis, who provided access to, and technical assistance with, electron microprobe and laser ablation ICP-MS analyses at the Max Planck Institute (Mainz, Germany) and Axel Schmitt (UCLA) for his help and assistance with zircon dating and preliminary evaluation of raw data. We thank the Smithsonian National Museum of Natural History (Washington, DC, USA) for providing us with the standards for electron microprobe analysis and J. Valley (University of Wisconsin) for the KIM-5 zircon standard for oxygen isotopes by SIMS. The insightful reviews of Olgeir Sigmarsson and one anonymous referee helped us to substantially improve the manuscript. Editorial handling of the paper by Timothy Grove is gratefully acknowledged. This work was supported by the NSF Grants EAR 0911093 to AAG and CAREER EAR 0805972 to IBN, by the Max Planck Society (Germany) and INSU-CNRS (France). This is CRPG contribution 2378.

References

Alt JC, Muehlenbachs K, Honnorez J (1986) An oxygen isotopic profile through the upper kilometer of the oceanic crust, DSDP Hole 504B. Earth Planet Sci Lett 80:217–229

Andersen DJ, Lindsley DH (1988) Internally consistent solution models for Fe–Mg–Mn–Ti oxides. Am Mineral 73:714–726

Andersen DJ, Lindsley DH, Davidson PM (1993) QUILF: a PASCAL program to assess equilibria among Fe–Mg–Ti oxides, pyroxenes, olivine and quartz. Comput Geosci 19:1333–1350

Best MG (2003) Igneous and metamorphic petrology. Blackwell Science Ltd, Oxford

Bindeman I (2008) Oxygen isotopes in mantle and crustal magmas as revealed by single crystal analysis. In: Putirka KD, Tepley III FJ (eds) Minerals, inclusions and volcanic processes. Rev Mineral Geochem 69, Mineral Soc Am. Washington DC, pp 445–478

Bindeman IN, Simakin AG (2014) Rhyolites—hard to produce, but easy to recycle and sequester: integrating microgeochemical observations and numerical models. Geosphere. doi:10.1130/GES00969.1

Bindeman IN, Valley JW (2002) Oxygen isotope study of the Long Valley magma system, California: isotope thermometry and convection in large silicic magma bodies. Contrib Mineral Petrol 144:185–205

Bindeman IN, Valley JW (2003) Rapid generation of both high- and low-$\delta^{18}O$, large-volume silicic magmas at the Timber Mountain/Oasis Valley caldera complex, Nevada. Geol Soc Am Bull 115:581–595

Bindeman I, Schmitt A, Valey JW (2006) U–Pb zircon geochronology of silicic tuffs from the Timber Mountain/Oasis Valley caldera complex, Nevada: rapid generation of large volume magmas by shallow-level remelting. Contrib Mineral Petrol 152:649–665

Bindeman IN, Gurenko AA, Sigmarsson O, Chaussidon M (2008a) Oxygen isotope heterogeneity and disequilibria of olivine phenocrysts in large volume basalts from Iceland: evidence for magmatic digestion and erosion of Pleistocene hyaloclastites. Geochim Cosmochim Acta 72:4397–4420

Bindeman IN, Fu B, Noriko KT, Valley JW (2008b) Origin and evolution of silicic magmatism at Yellowstone based on ion microprobe analysis of isotopically zoned zircons. J Petrol 49:163–193

Bindeman I, Gurenko A, Carley T, Miller C, Martin E, Sigmarsson O (2012) Silicic magma petrogenesis in Iceland by remelting of hydrothermally altered crust based on oxygen isotope diversity and disequilibria between zircon and magma with implications for MORB. Terra Nova 24:227–232

Blake S (1984) Magma mixing and hybridization processes at the alkalic, silicic, Torfajökull central volcano triggered by tholeiitic Veidivötn fissuring, south Iceland. J Volcanol Geotherm Res 22:1–31

Boehnke P, Watson EB, Trail D, Harrison TM, Schmitt AK (2013) Zircon saturation re-revisited. Chem Geol 351:324–334

Bourgeois O, Dauteuil O, Van Vliet-Lanoë B (1998) Pleistocene subglacial volcanism in Iceland: tectonic implications. Earth Planet Sci Lett 164:165–178

Bowen NL (1928) Origin of igneous rocks. Plinceton University Press, NewJersey

Carley TL, Miller CL, Barth AP, Bindeman IN, Wooden JL (2011) Zircon from historic eruptions in Iceland: reconstructing storage and evolution of silicic magmas. Mineral Petrol 102:135–161

Carmichael ISE (1964) The petrology of Thingmuli, a Tertiary volcano in eastern Iceland. J Petrol 5:435–460

Chacko T, Cole DR, Horita J (2001) Equilibrium oxygen, hydrogen and carbon isotope fractionation factors applicable to geologic systems. In: Valley JW, Cole DR (eds) Stable isotope geochemistry. Rev Mineral Geochem 43, Mineral Soc Am. Washington DC, pp 1–81

Chiba H, Chacko T, Clayton RN, Goldsmith JR (1989) Oxygen isotope fractionations involving diopside, forsterite, magnetite, and calcite: application to geothermometry. Geochim Cosmochim Acta 53:2985–2995

Condomines M, Grönvold K, Hooker PJ, Muehlenbachs K, O'Nions RK, Óskarsson N, Oxburgh ER (1983) Helium, oxygen, strontium and neodymium isotopic relationships in Icelandic volcanics. Earth Planet Sci Lett 66:125–136

Ferry J, Watson E (2007) New thermodynamic models and revised calibrations for the Ti-in-zircon and Zr-in-rutile thermometers. Contrib Mineral Petrol 154:429–437

Frost BR, Lindsley DH, Andersen DJ (1988) Fe–Ti oxide-silicate equilibria: assemblages with fayalitic olivine. Am Mineral 73:727–740

Furman T, Frey FA, Meyer PS (1992) Petrogenesis of evolved basalts and rhyolites at Austurhorn, southeastern Iceland: the role of fractional crystallisation. J Petrol 33:1405–1445

Gautason B, Muehlenbachs K (1998) Oxygen isotopic fluxes associated with high-temperature processes in the rift zones of Iceland. Chem Geol 145:275–286

Gerasimovsky VI, Polyakov AI, Durasova HF et al (1978) Iceland and the mid-Atlantic ridge, Geokhemistry. Nauka, Moscow

Getty SR, DePaolo DJ (1995) Quaternary geochronology using the U–Th–Pb method. Geochim Cosmochim Acta 59:3267–3272

Gillis KM, Coogan LA (2002) Anatectic migmatites from the roof of an ocean ridge magma chamber. J Petrol 43:2075–2095

Gregory RT, Taylor HP (1981) An oxygen isotope profile in a section of Cretaceous oceanic crust, Samail Ophiolite, Oman: evidence for $\delta^{18}O$ buffering of the oceans by deep (>5 km) seawater-hydrothermal circulation at mid-ocean ridges. J Geophys Res 86:2737–2755

Grimes C, Ushikubo T, John B, Valley J (2011) Uniformly mantle-like $\delta^{18}O$ in zircons from oceanic plagiogranites and gabbros. Contrib Mineral Petrol 161:13–33

Gunnarsson B, Marsh BD, Taylor HP (1998) Generation of Icelandic rhyolites: silicic lavas from the Torfajökull central volcano. J Volcanol Geotherm Res 83:1–45

Gurenko AA, Chaussidon M (2002) Oxygen isotope variations in primitive tholeiites of Iceland: evidence from a SIMS study of glass inclusions, olivine phenocrysts and pillow rim glasses. Earth Planet Sci Lett 205:63–79

Gurenko AA, Trumbull RB, Thomas R, Lindsay JM (2005) A melt inclusion record of volatiles, trace elements and Li–B isotope variations in a single magma system from the Plat Pays Volcanic Complex, Dominica, Lesser Antilles. J Petrol 46:2495–2526

Harrison TM, Watson EB, Aikman AB (2007) Temperature spectra of zircon crystallization in plutonic rocks. Geology 35:635–638

Hattori K, Muehlenbachs K (1982) Oxygen isotope ratios of the Icelandic crust. J Geophys Res 87:6559–6565

Hayden LA, Watson EB (2007) Rutile saturation in hydrous siliceous melts and its bearing on Ti-thermometry of quartz and zircon. Earth Planet Sci Lett 258:561–568

Hofmann AW (1988) Chemical differentiation of the Earth: the relationship between mantle, continental crust and oceanic crust. Earth Planet Sci Lett 90:297–314

Hoskin PWO, Schaltegger U (2003) The composition of zircon and igneous and metamorphic petrogenesis. In: Hanchar JM, Hoskin PWO (eds) Zircon. Rev Mineral Geochem 53, Mineral Soc Am, Washington DC, pp 27-62

Jakobsson S (1966) The Grimsnes lavas, SW-Iceland. Acta Nat Isl 2:5–30

Jakobsson SP (1972) Chemistry and distribution pattern of recent basaltic rocks in Iceland. Lithos 5:365–368

Jakobsson SP (1979) Petrology of recent basalts of the Eastern Volcanic Zone, Iceland. Acta Nat Isl 26:1–103

Jakobsson SP, Jónasson K, Sigurdsson IA (2008) The three igneous rock series of Iceland. Jökull 58:117–138

Jónasson K (2007) Silicic volcanism in Iceland: composition and distribution within the active volcanic zones. J Geodyn 43:101–117

Jørgensen KA (1980) The Thórsmörk ignimbrite: an unusual comenditic pyroclastic flow in southern Iceland. J Volcanol Geotherm Res 8:7–22

Jørgensen KA (1987) Mineralogy and petrology of alkaline granophyric xenoliths from the Thorsmörk ignimbrite, southern Iceland. Lithos 20:153–168

Lacasse C, Sigurdsson H, Carey SN, Jóhannesson H, Thomas LE, Rogers NW (2007) Bimodal volcanism at the Katla subglacial caldera, Iceland: insight into the geochemistry and petrogenesis of rhyolitic magmas. Bull Volcanol 69:373–399

Larsen JG (1979) Glass-bearing gabbro inclusions in hyaloclastites from Tindfjalljokull, Iceland. Lithos 12:289–302

Le Bas MJ, Streckeisen AL (1991) The IUGS systematics of igneous rocks. J Geol Soc 148:825–833

Le Bas MJ, Le Maitre RW, Streckeisen A, Zanettin B (1986) A chemical classification of volcanic rocks based on the total alkali-silica diagram. J Petrol 27:745–750

Lindsley DH (1983) Pyroxene thermometry. Am Mineral 68:477–493

Ludwig KR (2008) User's manual for Isoplot 3.70: a geochronological toolkit for Microsoft Excel. Berkeley Geochronology Center, Spec Publ No. 4, p 77

Macdonald R, Sparks RSJ, Sigurdsson H, Mattey DP, McGarvie DW, Smith RL (1987) The 1875 eruption of Askja volcano, Iceland: combined fractional crystallization and elective contamination in the generation of rhyolitic magma. Mineral Mag 51:183–202

Macdonald R, McGarvie DW, Pinkerton H, Smith RL, Palacz ZA (1990) Petrogenetic evolution of the Torfajökull volcanic complex, Iceland I. Relationship between the magma types. J Petrol 31:429–459

Marsh BD, Gunnarsson B, Congdon R, Carmody R (1991) Hawaiian basalt and Icelandic rhyolite: indicators of differentiation and partial melting. Geol Rundsch 80:481–510

Martin E, Sigmarsson O (2007) Crustal thermal state and origin of silicic magma in Iceland: the case of Torfajökull, Ljósufjöll and Snæfellsjökull volcanoes. Contrib Mineral Petrol 153:593–605

McBirney AR (2006) Igneous petrology. Jones and Bartlett, Sudbury

Miller CF, McDowell SM, Mapes RW (2003) Hot and cold granites? Implications of zircon saturation temperatures and preservation of inheritance. Geology 31:529–532

Muehlenbachs K, Anderson AT, Sigvaldason GE (1974) Low-^{18}O basalt from Iceland. Geochim Cosmochim Acta 38:577–588

Murphy MD, Sparks RSJ, Barclay J, Carroll MR, Lejeune A-M, Brewer TS, Macdonald R, Black S, Young S (1998) The role of magma mixing in triggering the current eruption at the Soufriere Hills Volcano, Montserrat, West Indies. Geophys Res Lett 25:3433–3435

Namur O, Charlier B, Toplis MJ (2011) Differentiation of tholeiitic basalt to A-type granite in the Sept Iles layered intrusion, Canada. J Petrol 52:487–539

Palmason G, Saemundsson K (1974) Iceland in relation to the mid-Atlantic ridge. Ann Rev Earth Planet Sci 2:25–50

Portnyagin M, Hoernle K, Storm S, Mironov N, van den Bogaard C, Botcharnikov R (2012) H_2O-rich melt inclusions in fayalitic olivine from Hekla volcano: implications for phase relationships in silicic systems and driving forces of explosive volcanism on Iceland. Earth Planet Sci Let 357–358:337–346

Prestvik T, Goldberg S, Karlsson H, Grönvold K (2001) Anomalous strontium and lead isotope signatures in the off-rift Öræfajökull central volcano in south-east Iceland—evidence for enriched endmember(s) of the Iceland mantle plume? Earth Planet Sci Lett 190:211–220

Sañudo-Wilhelmy SA, Flegal AR (1994) Temporal variations in lead concentrations and isotopic composition in the Southern California Bight. Geochim Cosmochim Acta 58:3315–3320

Schärer U (1984) The effect of initial 230Th disequilibrium on young U–Pb ages: the Makalu case, Himalaya. Earth Planet Sci Lett 67:191–204

Schattel N, Portnyagin M, Golowin R, Hoernle K, Bindeman I (2014) Contrasting conditions of rift and off-rift silicic magma origin on Iceland. Geophys Res Lett. doi:10.1002/2014GL060780

Schmitt AK, Grove M, Harrison TM, Lovera O, Hulen J, Walters M (2003) The Geysers—Cobb Mountain Magma System, California (Part 1): U–Pb zircon ages of volcanic rocks, conditions of zircon crystallization and magma residence times. Geochim Cosmochim Acta 67:3423–3442

Schmitt AK, Stockli DF, Hausback BP (2006) Eruption and magma crystallization ages of Las Tres Vírgenes (Baja California) constrained by combined $^{230}Th/^{238}U$ and (U–Th)/He dating of zircon. J Volcanol Geotherm Res 158:281–295

Sigmarsson O, Hémond C, Condomines M, Fourcade S, Óskarsson N (1991) Origin of silicic magma in Iceland revealed by Th isotopes. Geology 19:621–724

Sigmarsson O, Condomines M, Fourcade S (1992) A detailed Th, Sr and O isotope study of Hekla: differentiation processes in an Icelandic volcano. Contrib Mineral Petrol 112:20–34

Sigurdsson H (1968) Petrology of acid xenoliths from Surtsey. Geol Mag 105:440–453

Sigurdsson H (1977) Generation of Icelandic rhyolites by melting of plagiogranites in the oceanic layer. Nature 269:25–28

Sigurdsson H, Sparks R (1981) Petrology of rhyolitic and mixed magma ejecta from the 1975 eruption of Askja, Iceland. J Petrol 22:41–84

Stakes DS, Taylor HP (1992) The northern Samail ophiolite: an oxygen isotope, microprobe, and field study. J Geophys Res 97:7043–7080

Sverrisdottir G (2007) Hybrid magma generation preceding Plinian silicic eruptions at Hekla, Iceland: evidence from mineralogy and chemistry of two zoned deposits. Geol Mag 144:643–659

Taylor HPJ, Sheppard SMF (1986) Igneous rocks: I. Processes of isotopic fractionation and isotopic systematics. In: Valley JW, Taylor HPJ, O'Neil JR (eds) Stable isotopes in high temperature geological processes. Mineral Soc Amer 16. Washington DC, pp 227–271

Thy P, Beard JS, Lofgren GE (1990) Experimental constraints on the origin of Icelandic rhyolites. J Geol 98:417–421

Valley JW (2003) Oxygen isotopes in zircon. In: Hanchar JM, Hoskin PWO (eds) Zircon Rev Mineral Geochem 53, Mineral Soc Am. Washington DC, pp 343–385

Valley JW, Kitchen N, Kohn MJ, Niendorf CR, Spicuzza MJ (1995) UWG-2, a garnet standard for oxygen isotope ratios: strategies for high precision and accuracy with laser heating. Geochim Cosmochim Acta 59:5223–5231

Valley JW, Bindeman IN, Peck WH (2003) Empirical calibration of oxygen isotope fractionation in zircon. Geochim Cosmochim Acta 67:3257–3266

Valley J, Lackey J, Cavosie A, Clechenko C, Spicuzza M, Basei M, Bindeman I, Ferreira V, Sial A, King E, Peck W, Sinha A, Wei C (2005) 4.4 billion years of crustal maturation: oxygen isotope ratios of magmatic zircon. Contrib Mineral Petrol 150:561–580

Walker G (1966) Acid volcanic rocks in Iceland. Bull Volcanol 29:375–402

Watson EB (1996) Dissolution, growth and survival of zircons during crustal fusion: kinetic principles, geological models and implications for isotopic inheritance. Earth Sci 87:43–56

Watson EB, Harrison TM (1983) Zircon saturation revisited: temperature and composition effects in a variety of crustal magma types. Earth Planet Sci Lett 64:295–304

Watson EB, Harrison TM (2005) Zircon thermometer reveals minimum melting conditions on earliest Earth. Science 308:841–844

Watson EB, Wark DA, Thomas JB (2006) Crystallization thermometers for zircon and rutile. Contrib Mineral Petrol 151:413–433

Zhao Z-F, Zheng Y-F (2003) Calculation of oxygen isotope fractionation in magmatic rocks. Chem Geol 193:59–80

Zheng Y-F (1991) Calculation of oxygen isotope fractionation in metal oxides. Geochim Cosmochim Acta 55:2299–2307

Zheng Y-F (1993) Calculation of oxygen isotope fractionation in anhydrous silicate minerals. Geochim Cosmochim Acta 57:1079–1091